

AIR-MIST SPRAY MODEL DEVELOPMENT IN STEEL SECONDARY COOLING PROCESS

by

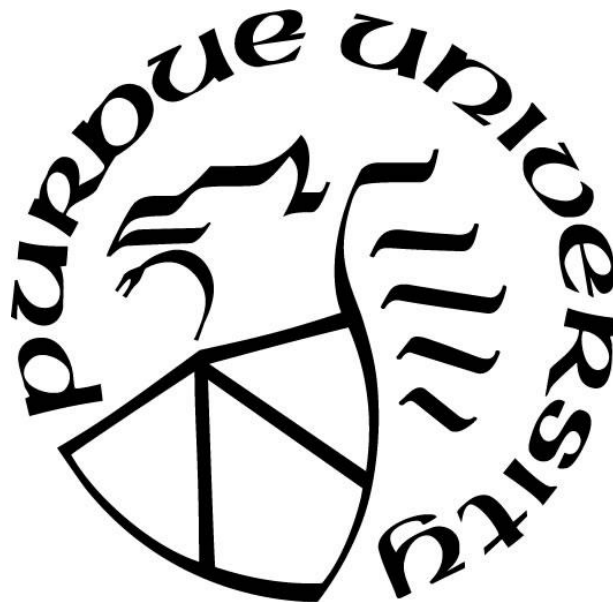
Edwin Andres Mosquera Salazar

A Thesis

Submitted to the Faculty of Purdue University

In Partial Fulfillment of the Requirements for the degree of

Master of Science in Mechanical Engineering



Department of Mechanical and Civil Engineering

Hammond, Indiana

May 2020

THE PURDUE UNIVERSITY GRADUATE SCHOOL
STATEMENT OF COMMITTEE APPROVAL

Dr. Chenn Q. Zhou, Chair

Department of Mechanical and Civil Engineering

Dr. Nesrin Ozalp

Department of Mechanical and Civil Engineering

Dr. Ran Zhou

Department of Mechanical and Civil Engineering

Approved by:

Dr. Chenn Q. Zhou Head of the Graduate Program

To Family, the ones who will always believe and love me

ACKNOWLEDGMENTS

I would like to thank the Steel Manufacturing Simulation and Visualization Consortium (SMSVC) for funding this project. The Center for Innovation through Visualization and Simulation (CIVS) at Purdue University Northwest is also gratefully acknowledged for providing all the resources required for this work. Last but not least, I appreciate the help and advice from Professor Chenn Zhou, Dr. Armin Silaen, and Haibo Ma, all great role models.

TABLE OF CONTENTS

TABLE OF CONTENTS.....	5
LIST OF TABLES.....	8
LIST OF FIGURES	9
ABSTRACT.....	11
CHAPTER 1. INTRODUCTION	12
1.1 Literature Review.....	13
1.1.1 Single-phase and two-phase nozzles	13
1.1.2 Spray characterization of nozzles and heat transfer	14
1.1.3 Atomization	15
1.1.4 VOF-to-DPM model.....	15
1.1.5 Mesh refinement adaptation methods.....	16
1.1.6 Mesh types	17
1.1.7 Turbulence models.....	17
1.2 Objectives	18
CHAPTER 2. METHODOLOGY AND CFD MODELS.....	19
2.1 Methodology	19
2.1.1 Cross-flow simulation.....	19
2.1.2 Air-mist nozzle simulation	20
2.2 CFD Models.....	22
2.2.1 Conservation of mass.....	22
2.2.2 Momentum equation.....	22
2.2.3 VOF model	22
2.2.3.1 Implicit scheme.....	23
2.2.3.2 Explicit scheme.....	23
2.2.4 Lagrangian model DPM	23
2.2.5 Breakup model.....	23
2.2.6 Nukiyama-Tanasawa distribution equation	25
2.2.7 Turbulence models.....	25
2.2.7.1 Realizable k-epsilon	25

2.2.7.2	SST k-omega	26
2.2.7.3	Large Eddy Simulation (LES)	27
2.2.7.4	Algebraic WMLES model	27
CHAPTER 3. CROSS-FLOW SIMULATION		28
3.1	Computational Domain and Boundary conditions.....	28
3.2	Results and Analysis	30
3.2.1	Effect of mesh adaptation methods.....	30
3.2.2	Effect of turbulence models	33
3.2.3	Effect of mesh resolution	36
3.3	Validation.....	36
CHAPTER 4. AIR-MIST NOZZLE SIMULATION		40
4.1	Nozzle internal region, Section 1 (VOF model)	40
4.1.1	Computational domain.....	40
4.1.2	Boundary conditions and fluid-gas properties	40
4.1.3	Effect of mesh types and mesh sensitivity study	41
4.1.4	Effect of operating conditions	44
4.1.5	Quasi-steady state of simulation cases	46
4.2	Spray formation region, Section 2	47
4.2.1	Computational domain and boundary conditions	47
4.2.2	Spray characterization (VOF model).....	50
4.2.3	Droplet generation methods.....	52
4.2.3.1	VOF-to-DPM model.....	52
4.2.3.2	Nukiyama-Tanasawa distribution equation model (DPM model).....	53
4.3	Validation.....	54
CHAPTER 5. AIR-MIST NOZZLES COMPARISON		57
5.1	Nozzle internal region, Section 1 (VOF model)	57
5.1.1	Computational domain and boundary conditions	57
5.1.2	Mesh sensitivity study	57
5.1.3	Air-mist nozzles comparison	59
5.1.4	Quasi-steady state of simulation cases	60
5.2	Spray characterization between nozzles, Section 2 (VOF model).....	61

CHAPTER 6. CONCLUSIONS.....	64
6.1 Cross-flow simulation.....	64
6.2 Air-mist nozzle simulation.....	64
REFERENCES	65
APPENDIX A. MATLAB CODE FOR INTERPOLATION FLUID-GAS PROPERTIES	68
APPENDIX B. RATIO APPROXIMATION TO FIND LIMITS IN CUMULATIVE VOLUME SIZE DISTRIBUTION	75
PUBLICATIONS.....	77

LIST OF TABLES

Table 1. Droplet size terminology [5]	14
Table 2. Turbulence models in Fluent.	18
Table 3. Fluid properties and boundary conditions of fluid and air phases.	30
Table 4. Mesh resolution and total droplet generated.	36
Table 5. Boundary conditions for simulation cases.	41
Table 6. Polyhedral mesh sensitivity study.....	43
Table 7. Conditions at the nozzle tip.	46
Table 8. Relations of operating conditions and velocity of the air-mist nozzle.	51
Table 9. Comparison measurement and CFD continuous at monitor location	52
Table 10. Performance of droplet generation methods.	55
Table 11. Validation for droplet size distribution.	56
Table 12. Polyhedral mesh sensitivity study.....	58
Table 13. Conditions at the nozzle tip.	60

LIST OF FIGURES

Figure 1. Schematic of continuous caster [1]	12
Figure 2. VOF-to-DPM transition model.....	20
Figure 3. Air-mist spray model.....	21
Figure 4. Droplet generation methodology.....	21
Figure 5. Cross-flow domain.	28
Figure 6. (a) Testing mesh, (b) Validation mesh.	29
Figure 7. (a) PUMA mesh adaptation, (b) VOF-to-DPM transition using WMLES S-Omega....	31
Figure 8. (a) Hanging Node Adaptation, (b) VOF-to-DPM transition using WMLES S-Omega.	32
Figure 9. Effect of mesh adaptation methods in droplet size distribution on plane 1.	32
Figure 10. (a) Velocity and liquid volume fraction, (b) VOF-to-DPM transition using WMLES S-Omega.	33
Figure 11. (a) Velocity and liquid volume fraction, (b) VOF-to-DPM transition using Realizable k-epsilon.....	34
Figure 12. (a) Velocity and liquid volume fraction, (b) VOF-to-DPM using SST k-omega.....	35
Figure 13. Effect of turbulence models in droplet size distribution on plane 1.....	35
Figure 14. PUMA mesh adaptation on XY cross-section midplane.....	37
Figure 15. Velocity magnitude and liquid VOF.	37
Figure 16. VOF-to-DPM transition.....	38
Figure 17. Validation for droplets size distribution.....	39
Figure 18. Section 1, Delavan Cool-Cast air-mist nozzle 3D geometry.....	40
Figure 19. Tetrahedral mesh using ANSYS, (b) Polyhedral mesh using STAR-CCM+.....	42
Figure 20. (a) Internal reference line (b) Velocity along the reference line for all surface remesher proximity factors.	43
Figure 21. Absolute pressure along the reference line.....	44
Figure 22. Velocity magnitude along the reference line.....	45
Figure 23. Water concentration VOF along the reference line.....	45
Figure 24. Monitor point.....	46
Figure 25. The convergence of the probe point at 20,000 iterations.	47
Figure 26. Section 2, spray region.	47

Figure 27. Polyhedral mesh, potential core area refined (500 μ m).....	48
Figure 28. (a) Potential core area refined (100 μ m), (b) Top view injection imprinted face.....	49
Figure 29. (a) Hexahedral mesh, (b) top view injection imprinted face (1mm).	49
Figure 30. Air-mist nozzles spray characterization.	50
Figure 31. CFD and test spray comparison.....	51
Figure 32. Normalized typical cumulative volume size distribution [5]	53
Figure 33. Air-mist spray velocity magnitude.	54
Figure 34. Comparison of droplet generation methods.	55
Figure 35. Cumulative volume size distribution for both methods.	56
Figure 36. Section 1, Spraying System Caster-Jet 3D model.	57
Figure 37. (a) Internal reference line, (b) Velocity along the reference line for all surface remesher proximity factors.	58
Figure 38. Absolute pressure along the reference line.....	59
Figure 39. Velocity magnitude along the reference line.....	59
Figure 40. Water concentration VOF along the reference line.	60
Figure 41. Monitor points.	61
Figure 42. The convergence of the probe point at 20,000 iterations.	61
Figure 43. Air-mist nozzles spray characterization.	62
Figure 44. Spray coverage at 190mm standoff distance.	63

ABSTRACT

Continuous casting is an important process to transform molten metal into solid. Arrays of spray nozzles are used along the process to remove heat from the slab letting it solidify. Efficient and uniform heat removal without slab cracking is desired during steel continuous casting, and air-mist sprays could help to achieve this goal. Air-mist nozzles are one of the important keys for determining the quality of steel as well as energy consumption for pumping the water. Based on industrial data, it is estimated that a 1% reduction in scrapped production due to casting related defects can result in annual savings of 40.53 million dollars in the U.S. Computational simulations studies can minimize defects in steel such as cracks, inclusions, macro-segregations, porosity, and others, which are closely related to the heat transfer between water droplets and hot slab surface.

Conducting multiple spray experiments in order to find optimum operating conditions might be impractical and expensive in some cases. Thus, Computational Fluid Dynamics (CFD) simulation is aimed to be used for simulating the air-mist spray process. Because it is a challenging process due to strong air and water interaction, then numerical models have been developed to simulate water droplets. The first model involves air and water phases which then are transformed in single-phase water droplets. To do so, a Volume of Fraction (VOF) to the Discrete Phase Model (DPM) is used.

VOF-TO-DPM transition model involves the primary and secondary breakup which occurs in the water atomization process, starting with a single water core, followed by a smaller compact mass of water known as lumps or ligaments due to the interaction of air, and finally converted into water droplets. The second model is using the Nukiyama-Tanasawa function size distribution which injects water droplets based on defined size range and velocity profile. A validation of droplet size and velocity against experimental data has been accomplished. The models can avoid acquiring expensive equipment in order to understand nozzle spray performance, and droplets generated. Quality, water droplet velocity, size, energy, and water consumption are the core of the current study. Last but not least, the methodology for this model can be used in any other air-mist nozzle design.

CHAPTER 1. INTRODUCTION

In the steel making, continuous casting is the process where molten steel is poured into a ladle, tundish and mould, see Figure 1. This process allows producing continuously ingots, slabs, blooms or billets [1] that will be later turned into structural parts, bars, rods, or coils. The casting speed mainly changes depending on the steel composition. Arrays of spray nozzles cool down the surface, removing heat as uniform as possible to avoid defective parts. The part is solidified at the end of the process. This thesis study focuses on the secondary cooling section, developing an air-mist nozzle model using CFD.

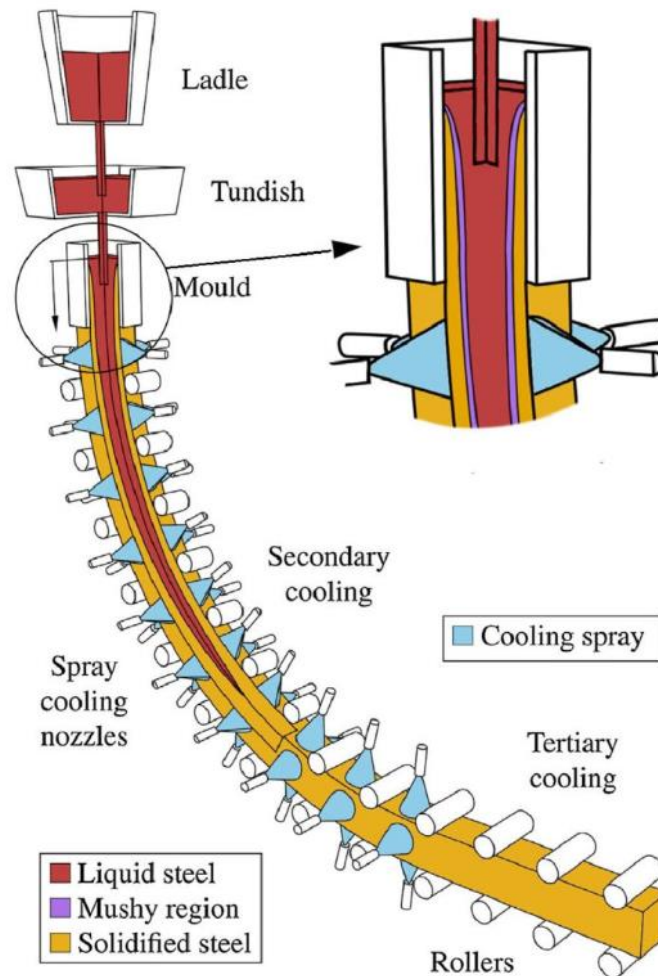


Figure 1. Schematic of continuous caster [1] .

1.1 Literature Review

1.1.1 Single-phase and two-phase nozzles

Under the same spray density conditions, single-phase e.g. hydraulic nozzle produces droplet size of the order of thousand microns and two-phase e.g. air-mist nozzle produces droplet size of the order of tens to hundreds of microns [2] . Smaller droplets can evaporate quicker, and it can reduce the water build-up under rolls. Another advantage of using air-mist nozzles is the innovative easy tip and tube replacement design, giving the chance to low downtime because of nozzle clogging and breakouts [2] . There are different droplet tests to measure velocity, pressure, uniformity, and size. For instance, impact test can be calculated using theoretical formulas without considering the turbulence, conducting experiments is important to calculate impact force, lateral distribution, and transverse distribution on the covered area that is being tested [2] . A force transducer is used for scanning the impact pressure from droplets impinging a surface [3] .

Delavan Cool-Cast W19917-15 is the flat fan air-mist nozzle used for this research. The spray characterization for this nozzle was tested using a two-dimensional system Artium Technologies Phase Doppler Interferometry (PDI)-300MD. Industrial collaborators conducted tests, and details about the laser types and positions of the receiver and transmitter cannot be disclosed from the experiment. Drop size and velocity measurements were obtained using these tests. Another test to collect data is the Phase Doppler Particle Analyzer (PDPA) test which can go from agriculture application to a natural disaster like a hurricane [4] . Droplet size terminology can be seen in Table 1 [5] . Computational Fluid Dynamics (CFD) simulations can be also used to optimize the spraying, collected experimental data is used as input for the simulation in order to improve the accuracy, velocity, pressure, turbulence, flow patterns, and droplets trajectories, among others variables, can be obtained from CFD analysis [2] .

Table 1. Droplet size terminology [5] .

Terminology	Definition
$D_{V0.1}$	10 % of total liquid volume or mass has diameters smaller or equal to it
D_{32}	Sauter mean diameter (SMD) has the same volume to surface area ratio
$D_{V0.5}$	The volume mean diameter (VMD) 50 % of total liquid volume or mass has diameters larger than the median value and 50 % smaller than the median value
$D_{V0.9}$	90 % of total liquid volume or mass has diameters smaller or equal to it

1.1.2 Spray characterization of nozzles and heat transfer

Steady-state and transient experimental methods are used to measure the heat transfer coefficient (HTC) from mist nozzles to steel surface as seen in [3] . Air-mist nozzles produce high droplet velocities compared to hydraulic nozzles due to their gas flow fields. The stationary slab experiment did not show realistic cooling results in the mill. Also, cooling efficiency decreases when casting velocity increases. Mean HTC increases when water pressure increases. Experimental HTCs varying steel chemistry and using an air-mist nozzle, a standoff distance of 190 mm, the water flow rate of 21.2 l/min, and air pressure of 2.1 bars were used as experimental conditions [6] . Experimental conditions of steel temperature at 1200 °C, air pressure of 2 bars, and water pressure of 0.5 bars with its corresponding HTCs were illustrated in [7] .

An HTC drop in the overlapped area was reported. Ramstorfer, etc. conducted experiments with steel surface temperature at 1250 °C with sets of different air-mist nozzle operating conditions [8] . Findings reported that jet velocity does not influence the cooling. Therefore, a new correlation was proposed, stating that the heat transfer coefficient is $\alpha = a q^b$ where q is water flux and a , and b are coefficients found from the experiment. Zhang, etc. run an experiment to measure air-mist nozzle velocity profiles using particle image velocimetry (PIV) and laser doppler velocimetry (LDV) [9] . A higher particle concentration was found close to the nozzle outlet tip, predicting the potential core breakup. A comparison for both measurement techniques

was plot using air pressure of 0.2 MPa and water pressure of 0.4 MPa. Also, a velocity distribution equation was proposed describing the entire flow field.

Cheng, etc. conducted Eulerian multiphase CFD simulations using a prototype nozzle [10] . The boundary condition for air inlet was chosen as pressure inlet while water inlet as mass flow inlet. Liquid fractions at nozzle outlet were found between 0.07 and 0.3; depending on the simulated conditions. Moreover, increasing the air pressure, increases water droplets velocity, while increasing the water pressure, decreases water droplets velocity. Vashahi, etc. simulated a CFD case, using the VOF method where a pressure swirl nozzle with 8.7 million hex cells from the internal and external nozzle was used in order to predict accurately the swirling flow [11] .

1.1.3 Atomization

Arthur, etc claims basic process that governs the development of emerging liquid stream, its disintegration into ligaments and droplets. Also, spray characterization depends on the internal geometry and physical properties of the liquid and gas medium [12] . Moreover, different functions allow coming up with mathematical representations of measured droplet size distribution; among them are normal, log-normal, Nukiyama-Tanasawa, Rosin-Rammler, and upper limit distribution. Nukiyama-Tanasawa is a function that has four independent constants that allow capturing multiple distributions compared to other functions that use two parameters such as Rosin-Rammler [12] . STAR-CCM+ 13.04.010 has the Nukiyama-Tanasawa droplet size generator model and this states that typical uses are in high speed liquid sprays in IC engines [13] . Accurate distribution of droplet size is a very important parameter for analysis of mass and heat transport [14] -- [15] . Also, researchers have used Nukiyama-Tanasawa concluding that droplet size distribution showed good agreement with samples studied [14] -- [16] .

1.1.4 VOF-to-DPM model

Volume of Fluid (VOF) and Discrete Phase Model (DPM) has been tried to be coupled in the past by other researchers. There are some disadvantages if models are run separately. For example, simulating all length scales at once in a spray in a jet engine can be inefficient and impractical if there is not a consideration of domain size and cell size of the order of microns [17] . Also, a lower-cost strategy can be using DPM by tracking Lagrangian particles;

nevertheless, droplets can be adequately computed far from the solid-liquid core in the dispersed region, but they cannot be captured accurately near the liquid core.

The hybridization of two models into a single spray modeling technique using an algorithm of droplet identification based on Connected Components Labeling (CCL) was proposed in [17] . Coupled Level Set and Volume of Fluid (CLSVOF) and the DPM Lagrangian tracking using adaptive mesh refinement were simulated in [18] . Where neighbor search algorithms were used on the finest refinement level in order to find candidates droplets for the DPM tracking from the liquid-gas interfaces in the Eulerian domain. Furthermore, an extensive explanation of CPU time based on mesh resolutions for validated cases were also reported. ANSYS FLUENT 19.1 illustrates in [19] the VOF-to-DPM transition criteria when the lumps are close to a spherical shape, considering 0 as a perfect sphere for asphericity. A normalized standard deviation by the average radius will be calculated between facets center on each lump with respect to its center of gravity. Moreover, average radius-surface orthogonality will be calculated from the relative orthogonality of every facet of the lump surface. A split factor definition is introduced in ANSYS Fluent webinar [20] ; this input factor can either create more or fewer parcels if the DPM parcel exceeds the cell volume.

1.1.5 Mesh refinement adaptation methods

Hanging Node Adaptation and Polyhedral Unstructured Mesh Adaptation (PUMA) are mesh refinement adaptation methods. Hanging Node Adaptation and PUMA will refine or coarsen the cell from the node that is not vertices of all sharing cells [21] . Also, the Hanging Node Adaptation method consumes more memory in order to maintain the mesh hierarchy and store temporary edges in 3D. In contrast, PUMA consumes less memory. Mesh cannot be coarsened further than the original cell size for both methods. PUMA can refine all cell types while Hanging Node Adaptation can refine all cell types but polyhedral. Gradient adaptation with water volume fraction as the variable can set a coarsen threshold and a refine threshold. Values above the refine threshold will be refined and values below coarsen one will be coarsened [22] . This is applicable for both adaptive methods. Both methods can either use the first gradient or second gradient; gradient or curvature respectively, depending if the simulated case involves a strong shock or smooth solution.



1.1.6 Mesh types

Using structured or unstructured grids depends indirectly on the simulation case that is trying to be accomplished, considering accuracy and efficiency. Polyhedral mesh is derived from tetrahedral mesh according to [23] ; polygons will be formed around each node in the tetrahedral mesh. Polyhedral mesh can also achieve faster converge solutions than Hexahedral and Tetrahedral mesh, again depending of the case. Tetrahedral mesh contains approximately five times more cells than a polyhedral mesh [23] -- [24] . Also, some meshing controls can be changed when doing the mesh. For instance, a growth factor less than 1 will create a slower cell growth, having more elements, leading a more dense mesh. Another control to increase the number of faces and cells is surface remesher proximity where the value of number points in a gap can be modified to create more or less faces, resulting in local refinements in the domain. Quality can also be checked after the mesh is completed, showing the smoothness between cells. Wake refinement allows the user to define a direction, distance, size and spread angle with respect to a part surface where the refinement will take place.

1.1.7 Turbulence models

Table 2 shows the turbulence models and the increment in computational time [25] . Reynolds-Averaged Navier Stokes (RANS) solve a time-averaged flow solution while Large Eddy Simulation (LES) solves for larger eddies, and models for smaller eddies in the solution. Three turbulence models were used for this research. Realizable $k-\varepsilon$ is more robust compared to Standard $k-\varepsilon$; it can be used when flows involve rotation, boundary layers, separation, and recirculation. Wall functions can be used to resolve the turbulence near the wall after checking the corresponding y^+ which is the dimensionless wall distance. SST $k-\omega$ is a hybrid model which combines outer layer (wake and outward) and inner layer (sub-layer, log-layer) into a blended law of the wall. WMLES S-Omega is an enhance the subgrid-scale model to capture the LES portion using the absolute difference of strain rate (S) and vorticity magnitude (Ω) [22] .

Table 2. Turbulence models in Fluent.

RANS based models	One-Equation Model Spalart-Allmaras	 Increase in Computational Cost Per Iteration 
	Two-Equation Models Standard k- ϵ RNG k- ϵ Realizable k- ϵ	
	Standard k- ω SST k- ω	
	4-Equation v2f*	
	Reynolds Stress Model	
	k-kl- ω Transition Model SST Transition Model	
	Detached Eddy Simulation Large Eddy Simulation	

1.2 Objectives

Current work for numerical simulation focuses on the development of an air-mist spray model. Proposing a three-step methodology to simulate the actual air-mist spray. Evaluating two approaches to generate droplets using either the VOF-to-DPM transition model or the Nukiyama-Tanasawa distribution function. Also, validation of droplet size and droplet velocity magnitude against literature and experiment are included in this research.

CHAPTER 2. METHODOLOGY AND CFD MODELS

Hydraulic nozzles and air-mist nozzles are used in steel continuous casters during the secondary cooling region. This research emphasizes air-mist nozzles because of the advantages stated in CHAPTER 1. It has not been published a full methodology to simulate air-mist nozzles. To do so, a cross-flow example has been used as a foundation simulation to test the VOF-to-DPM transition model, the effects of turbulence models, mesh adaptation methods, and mesh resolution. Then, the transition model and Nukiyama-Tanasawa distribution function have been implemented in simulating a flat fan Cool-Cast W19917-15 air-mist nozzle that has been used in the industry. This methodology is currently being applied to a second flat fan Spraying System Caster-Jet 50070 air-mist nozzle.

2.1 Methodology

2.1.1 Cross-flow simulation

A cross-flow example adopted from the work by Xiaoyi et al. [18] was used as a benchmark simulation to test the VOF-to-DPM transition model. The cross-flow simulation involves liquid and air phases, taking care by the VOF model. Because of the presence of the air stream, the liquid atomization process breakup can occur. Figure 2 illustrates simply how this model works. This model is activated from VOF-to-DPM when a liquid lump or ligament has a shape close to a sphere and size based on given user input. When these occur a liquid lump will take a spherical shape using the DPM model and its liquid phase in the cell in the continuous domain will be replaced by the second phase that is air. If mesh adaptive is used to help to achieve droplets certain size, then after the transition the cell can be coarsened back to reduce computation effort.

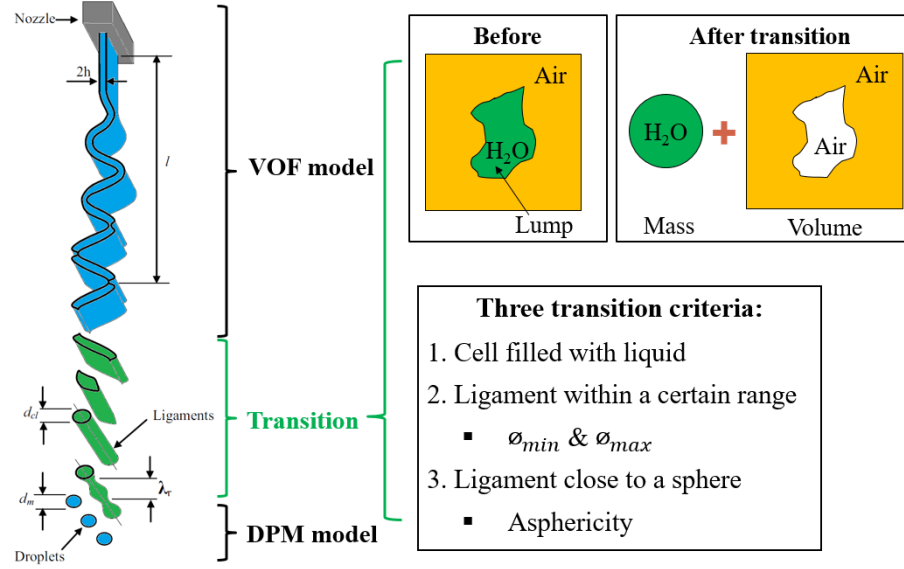


Figure 2. VOF-to-DPM transition model.

2.1.2 Air-mist nozzle simulation

Figure 3 shows the methodology to simulate an air mist nozzle being separated into three independent but linked sections. It was considered that way because of computational time, seeing the sections as a complete spray process. Section 1 uses the VOF method because of the presence of air gas and water liquid phases interacting inside the air-mist nozzle. When numerical solution achieves quasi-steady state, gas-liquid distribution and velocities components will be used as an injection profile at a fixed reference location near the nozzle tip leading the analysis to section 2. Thus, spraying going through the primary and secondary breakup will occur where the VOF-to-DPM transition model will be used. DPM model will be used in section 3 to continue the spray simulation using droplets size distribution and velocities components. Water droplets will eventually impinge a hot slab surface in order to remove heat; however, this research neglect the heat transfer analysis and focuses on simulating air-mist nozzle spray development.

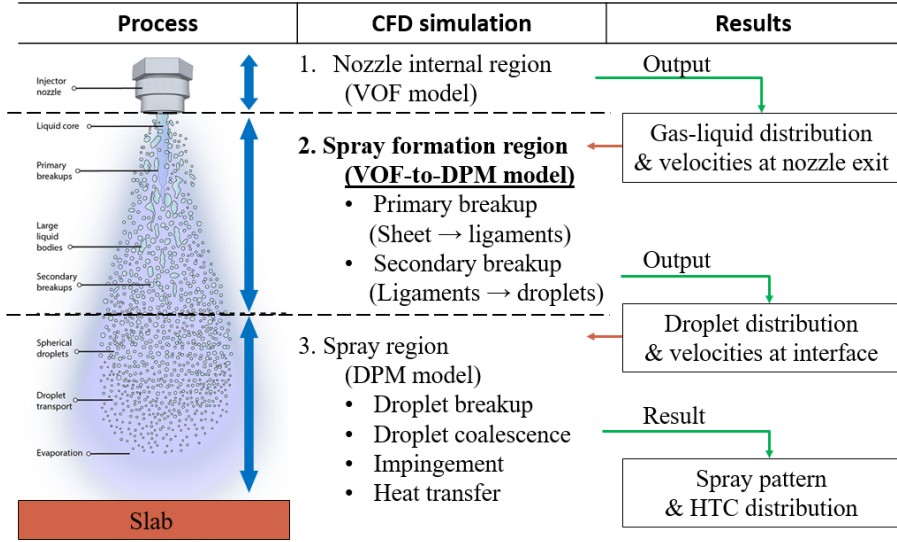


Figure 3. Air-mist spray model.

The VOF-to-DPM transition model is able to convert the liquid phase into liquid droplet. A second option to generate droplets can be using distribution equations, in this research Nukiyama-Tanasawa will be used, see Figure 4.

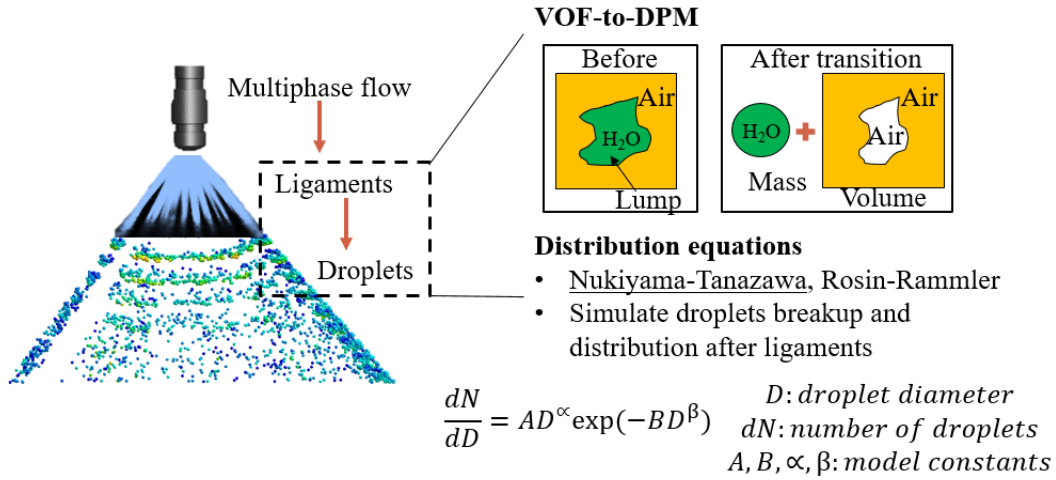


Figure 4. Droplet generation methodology.

2.2 CFD Models

Three-dimensional numerical simulations for both cross-flow and air-mist nozzle have been developed using the following equations and models. Mass and heat transfer between slab and liquid droplet has been neglected for current work.

2.2.1 Conservation of mass

$$\frac{D\rho}{Dt} + \rho \nabla \cdot \vec{v} = 0 \quad (1)$$

2.2.2 Momentum equation

Velocity will be shared between phases. However, accuracy near the phase's interface can be affected with larger velocity differences bringing into consideration to select the appropriate interface capturing scheme.

$$\frac{\partial}{\partial t}(\rho \vec{v}) + \nabla \cdot (\rho \vec{v} \vec{v}) = -\nabla p + \nabla \cdot [\mu(\nabla \vec{v} + \nabla \vec{v}^T)] + \rho \vec{g} + \vec{F} \quad (2)$$

2.2.3 VOF model

Tracking phases is accomplished after solving the continuity equation for the volume fraction of phases.

$$\frac{1}{\rho_q} \left[\frac{\partial}{\partial t} (\alpha_q \rho_q) + \nabla \cdot (\alpha_q \rho_q \vec{v}_q) \right] = \sum_{p=1}^n (\dot{m}_{pq} - \dot{m}_{qp}) \quad (3)$$

Where the mass transfer from phase q to phase p is \dot{m}_{qp} , and mass transfer from phase p to phase q is \dot{m}_{pq} . Volume fraction can be solved using implicit or explicit discretization in order to solve face fluxes between cells.

2.2.3.1 Implicit scheme

$$\frac{\alpha_q^{n+1} \rho_q^{n+1} - \alpha_q^n \rho_q^n}{\Delta t} V + \sum_f (\rho_q^{n+1} U_f^{n+1} \alpha_{q,f}^{n+1}) = [\sum_{p=1}^n (\dot{m}_{pq} - \dot{m}_{qp})] V \quad (4)$$

Volume fraction is calculated iteratively at each time step. This scheme works with transient and steady-state solutions.

2.2.3.2 Explicit scheme

$$\frac{\alpha_q^{n+1} \rho_q^{n+1} - \alpha_q^n \rho_q^n}{\Delta t} V + \sum_f (\rho_q^n U_f^n \alpha_{q,f}^n) = [\sum_{p=1}^n (\dot{m}_{pq} - \dot{m}_{qp})] V \quad (5)$$

Volume fraction is calculated at the previous time step. $\alpha_{q,f}$ is the face value of qth volume fraction computed from chose scheme, V is the volume of the cell, and U_f is the volume flux through the normal velocity on the face. Phases interface needs to be interpolated using different available schemes.

2.2.4 Lagrangian model DPM

Particles, which in this case are droplets, are subjected to different sort of forces.

$$m_p \frac{dv_p}{dt} = F_d + F_g \quad (6)$$

2.2.5 Breakup model

An alternative to the TAB model that is appropriate for high-Weber-number flows is the WAVE breakup model of Reitz [26] , which considers the breakup of the droplets to be induced by the relative velocity between the gas and liquid phases. The model assumes that the time of break up and the size of resulting droplets are related to the fastest-growing Kelvin-Helmholtz instability ($We > 100$), derived from the jet stability analysis described below. The wavelength and growth rate of this instability are used to predict details of the newly-formed droplets.

In the WAVE model, break up of droplet parcels is calculated by assuming that the radius of the newly-formed droplets is proportional to the wavelength of the fastest-growing unstable surface wave on the parent droplet:

$$r = B_0 \Lambda \quad (7)$$

where B_0 is a model constant set equal to 0.61 based on the work of Reitz [26] . Furthermore, the rate of change of droplet radius in the parent parcel is given by

$$\frac{da}{dt} = -\frac{(a-r)}{\tau} \quad (8)$$

where the break up time, τ , is given by

$$\tau = \frac{3.726 B_1 a}{\Lambda \Omega} \quad (9)$$

The break up time constant, B_1 , can range between 1 and 60, depending on the injector characterization. In this study, B_1 is set to a value of 1.73 as recommended by Liu et al. [27] .

The maximum growth rate Ω and the corresponding wavelength Λ are given by

$$\Omega \sqrt{\frac{\rho_1 a^3}{\sigma}} = \frac{0.34 + 0.38 We^{1.5}}{(1 + Oh)(1 + 1.4 Ta^{0.6})} \quad (10)$$

Where Ohnesorge number, Taylor number, and Weber number are defined as

$$Oh = \frac{\sqrt{We}}{Re} \quad (11)$$

$$Ta = Oh \sqrt{We} \quad (12)$$

$$We = \frac{\rho v_p^2 d}{\sigma} \quad (13)$$

In the WAVE model, mass is accumulated from the parent drop at a rate given by break up time τ until the shed mass is equal to 5% of the initial parcel mass. At this time, a new parcel is created with a new radius. The new parcel is given the same properties as the parent parcel with the exception of radius and velocity. The new parcel is given a component of velocity randomly selected in the plane orthogonal to the direction vector of the parent parcel, and the momentum of the parent parcel is adjusted so that momentum is conserved. The velocity magnitude of the new parcel is the same as the parent parcel.

2.2.6 Nukiyama-Tanasawa distribution equation

$$\frac{dN}{dD} = AD^\alpha \exp(-BD^\beta) \quad (14)$$

Where D: droplet diameter, dN: number of droplets, and A, B, α , β are model constants.

2.2.7 Turbulence models

The following turbulence models were tested.

2.2.7.1 Realizable k-epsilon

$$\frac{\partial(\rho k)}{\partial t} + \frac{\partial}{\partial x_j}(\rho k u_j) = \frac{\partial}{\partial x_j} \left[\left(\mu + \frac{\mu_t}{\sigma_k} \right) \frac{\partial k}{\partial x_j} \right] + G_k + G_b - \rho \varepsilon + Y_M + S_k \quad (15)$$

$$\frac{\partial(\rho \varepsilon)}{\partial t} + \frac{\partial}{\partial x_j}(\rho \varepsilon u_j) = \frac{\partial}{\partial x_j} \left[\left(\mu + \frac{\mu_t}{\sigma_\varepsilon} \right) \frac{\partial \varepsilon}{\partial x_j} \right] + \rho C_1 S \varepsilon - \rho C_2 \frac{\varepsilon^2}{k + \sqrt{\nu \varepsilon}} + C_{1\varepsilon} \frac{\varepsilon}{k} C_3 G_b + S_\varepsilon \quad (16)$$

$$C_1 = \max \left[0.43, \frac{\eta}{\eta + 5} \right], \eta = S \frac{k}{\varepsilon}, S = \sqrt{2 S_{ij} S_{ij}} \quad (17)$$

Standard wall functions for momentum boundary condition.

$$u^* = \begin{cases} y^* & (y^* < y_v^*) \\ \frac{\ln(Ey^*)}{k} & (y^* > y_v^*) \end{cases} \quad \begin{aligned} u^* &= \frac{u_p C_\mu^{\frac{1}{4}} k_p^{\frac{1}{2}}}{u_\tau^2} \\ y^* &= \frac{\rho C_\mu^{\frac{1}{4}} k_p^{\frac{1}{2}} y_p}{\mu} \end{aligned} \quad (18)$$

2.2.7.2 SST k-omega

$$\rho \frac{Dk}{Dt} = \tau_{ij} \frac{\partial \bar{u}_i}{\partial x_j} - \rho \beta^* f_{\beta^*} k \omega + \frac{\partial}{\partial x_j} \left[\left(\mu + \frac{\mu_t}{\sigma_\varepsilon} \right) \frac{\partial k}{\partial x_j} \right] \quad (19)$$

$$\mu_t = \alpha^* \rho \frac{k}{\omega} \quad (20)$$

$$\rho \frac{D\omega}{Dt} = \alpha \frac{\omega}{k} \tau_{ij} \frac{\partial \bar{u}_i}{\partial x_j} - \rho \beta f_\beta \omega^2 + \frac{\partial}{\partial x_j} \left[\left(\mu + \frac{\mu_t}{\sigma_\omega} \right) \frac{\partial \omega}{\partial x_j} \right] \quad (21)$$

Ω represents the specific dissipation rate.

$$\omega \approx \frac{\varepsilon}{k} \alpha \frac{1}{\tau} \quad (22)$$

Blended law of the wall equations

$$\rho \frac{Dk}{Dt} = \tau_{ij} \frac{\partial \bar{u}_i}{\partial x_j} - \rho \beta^* k \omega + \frac{\partial}{\partial x_j} \left[\left(\mu + \frac{\mu_t}{\sigma_k} \right) \frac{\partial k}{\partial x_j} \right] \quad (23)$$

$$\rho \frac{D\omega}{Dt} = \frac{\gamma}{v_t} \tau_{ij} \frac{\partial \bar{u}_i}{\partial x_j} - \rho \beta \omega^2 + \frac{\partial}{\partial x_j} \left[\left(\mu + \frac{\mu_t}{\sigma_\omega} \right) \frac{\partial \omega}{\partial x_j} \right] + 2\rho(1 - F_1)\sigma_{\omega^2} \frac{1}{\omega} \frac{\partial k}{\partial x_j} \frac{\partial \omega}{\partial x_j} \quad (24)$$

$$\Phi = F_1 \Phi_1 + (1 - F_1) \Phi_2 \quad \Phi = \beta, \sigma_k, \sigma_\omega, \gamma \quad (25)$$

2.2.7.3 Large Eddy Simulation (LES)

$$u_i(x, t) = \bar{u}_i(x, t) + u'_i(x, t) \quad (26)$$

Where u_i is the instantaneous component, \bar{u}_i is the resolved scale and u'_i is the subgrid-scale.

$$\frac{\partial u_i}{\partial t} + \frac{\partial(u_i u_j)}{\partial x_j} = -\frac{1}{\rho} \frac{\partial p}{\partial x_j} + \frac{\partial p}{\partial x_j} \left(\nu \frac{\partial u_i}{\partial x_j} \right) \quad (27)$$

Filtered N-S equation

$$\frac{\partial \bar{u}_i}{\partial t} + \frac{\partial(\bar{u}_i \bar{u}_j)}{\partial x_j} = -\frac{1}{\rho} \frac{\partial \bar{p}}{\partial x_j} + \frac{\partial p}{\partial x_j} \left(\nu \frac{\partial \bar{u}_i}{\partial x_j} \right) - \frac{\partial \tau_{ij}}{\partial x_j} \quad (28)$$

Subgrid scale Turbulent stress

$$\tau_{ij} = \rho(\overline{u_i u_j} - \bar{u}_i \bar{u}_j) \quad (29)$$

2.2.7.4 Algebraic WMLES model

$$\nu_t = \min \left[(k d_w)^2, (C_{smag} \Delta)^2 \right] S \left\{ 1 - \exp \left[- \left(\frac{y^+}{25} \right)^3 \right] \right\} \quad (30)$$

Where wall distance is d_w , the strain rate is S , $k=0.41$, $C_{smag}=0.2$, and y^+ is normal to the wall inner scaling.

$$\Delta = \min(\max(C_w d_w; C_w h_{max}, h_{wn}); h_{max}) \quad (31)$$

Where h_{max} is maximum edge length, h_{wn} is the wall normal grid spacing, and C_w is equal to 0.15.

CHAPTER 3. CROSS-FLOW SIMULATION

3.1 Computational Domain and Boundary conditions

The computational domain and the boundary conditions reported by Xiaoyi et al. [18] were used for the cross-simulation. Figure 5 shows the rectangular domain with dimensions in mm. Two different mesh resolutions were used to conduct different analyses and validation of the VOF-to-DPM transition model using ANSYS FLUENT 19.1, see Figure 6. The hexahedral type of mesh with a starting testing mesh resolution of $41 \times 21 \times 21$ nodes and 5 levels of cell refinement will not be used for validation purposes because this mesh can be considered still coarse after refinements, having an initial cell size of $1249\mu\text{m}$ and after refinements, the cell is $39\mu\text{m}$. Thus, this testing mesh will be used for evaluating the effects of different mesh refinement adaptation methods and turbulence models. Using mesh refinement methods is a technique to accurately simulate the VOF liquid ligament transition criteria for size and shape converted to liquid droplet DPM. A mesh resolution of $128 \times 64 \times 64$ nodes shows an ideal initial cell size of $400\mu\text{m}$ in all directions and using 5 levels of cell refinement in order to obtain a minimum cell size of $12.5\mu\text{m}$ for validation purposes.

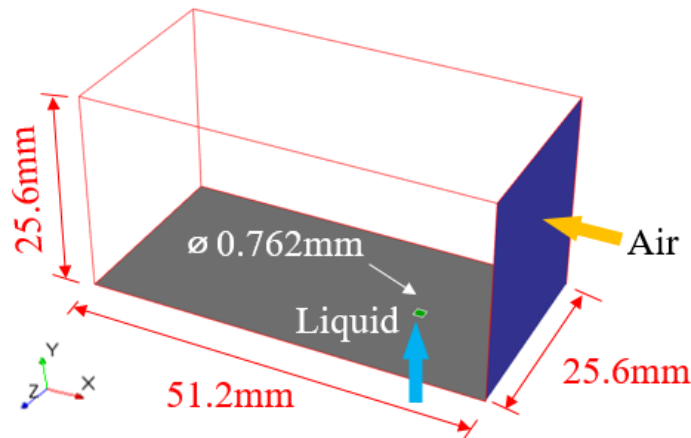


Figure 5. Cross-flow domain.

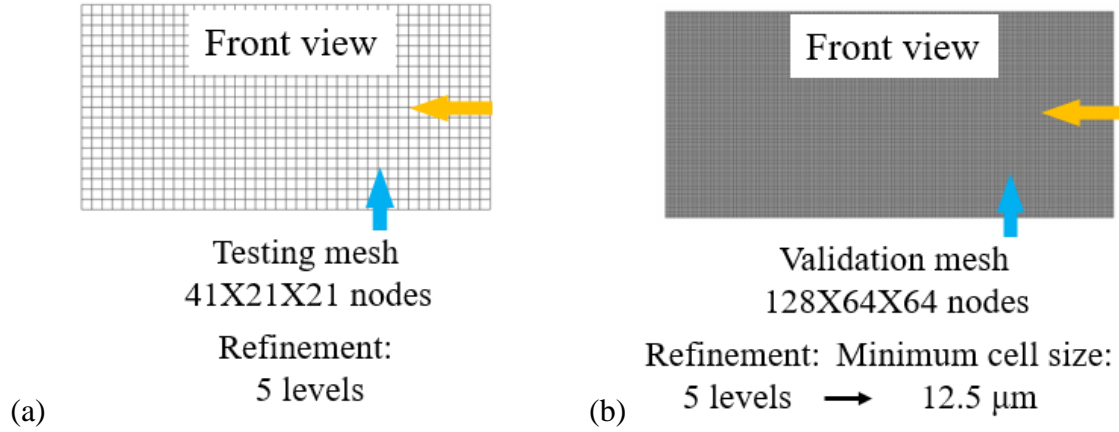


Figure 6. (a) Testing mesh, (b) Validation mesh.

Table 3 shows the fluid properties, the strong velocity magnitude for the air stream and the mass flow rate of the liquid that were used for simulations. The air stream is coming from the side and it was set as a velocity boundary condition, the injection location for liquid is 12.8mm downstream the air boundary. The boundary wall on the XZ plane of the liquid injection was set as a no-slip condition, remaining boundaries were set to outflows. Air constant gas properties are referenced at room and atmospheric conditions. A liquid jet Reynolds number of 5464 was calculated, so different turbulence models were used for the transient gas-liquid interaction simulation cases.

Because transition criterion from VOF-to-DPM is based on user input, a minimum and maximum droplet size of 0 to 200 μm was used for the testing mesh. On the other hand, a minimum and maximum droplet size of 0 to 50 μm , and 0 to 200 μm were used for the validation mesh. The shape is the second transition criterion, thus remembering that 0 will describe a perfect sphere while at a value of 1 the VOF lump cannot be a good candidate for DPM, then a value of 0.5 for radius standard deviation and radius-surface orthogonality was used. A split parcel ratio of 10 was used to break droplet parcels into more droplets generating a size distribution.

The cell refinement uses a curvature and standard lower and upper liquid volume fraction threshold of 1×10^{-10} and 1×10^{-8} , evaluating when the cell can either coarsen or refine according

to the mesh adaption method being used. Furthermore, explicit VOF-Geo-Reconstruct sharp interface model, no DPM interaction with the continuous phase, stochastic collision, coalescence and wave breakup were also activated. DPM interaction with the continuous phase was deactivated. The flow was initialized with -69m/s in X velocity. A time step of 1×10^{-6} seconds was used for testing mesh, and 1×10^{-7} seconds was used for validation mesh.

Table 3. Fluid properties and boundary conditions of fluid and air phases.

ρ_L	780 kg/m ³
σ_L	0.024 N/m
μ_L	0.0013 kg/m · s
\dot{m}_L	15.3 kg/h
u_A	69 m/s

3.2 Results and Analysis

Several studies were needed before conducting the validation. To do so, the testing mesh resolution from Figure 6 was used to come up with an accurate method and get more familiar to simulate the VOF-to-DPM transition using the cross-flow example. Simulations were run to 1.686ms.

3.2.1 Effect of mesh adaptation methods

One of the methods to simulate a specific droplet size can be by refining areas of interest within the domain close to a cell size compared to a droplet size; however, it results impractical in some cases because an excessive mesh is obtained in the domain. Another method is by using mesh adaptation techniques which were covered in CHAPTER 1. Liquid VOF was used as the variable for coarsen and refine thresholds. Figure 7 and Figure 8 show the effect of using PUMA and Hanging Node Adaptation in the cross-section XY midplane. Even though the same turbulence model, WMLES S-Omega, was used for both simulations, there are some differences in the liquid atomization process keeping in mind that the PUMA scheme consumed less memory.

Droplet size distributions for both mesh adaptation methods can be seen in Figure 9. Both results were compared to the results reported by Xiaoyi et al. [18] using a maximum droplet diameter as $200\mu\text{m}$ for the transition criteria. Results for both adaptation methods show larger droplet size distribution and this is because the current mesh resolution can be considered still coarse.

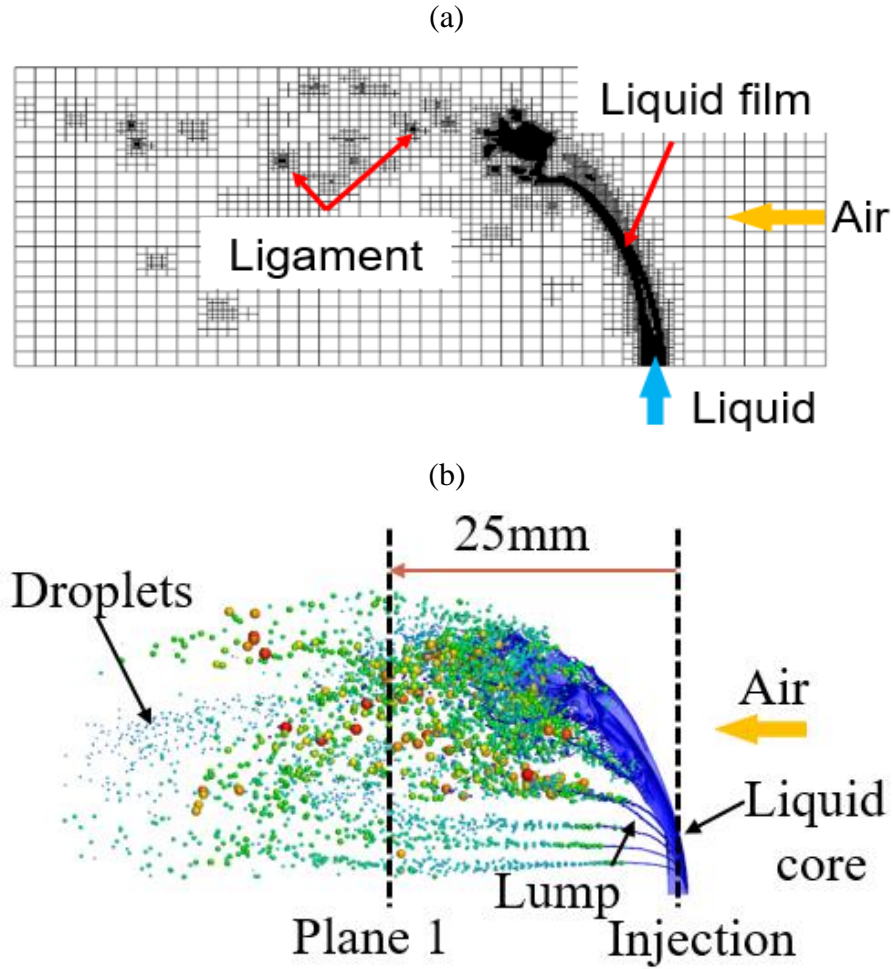


Figure 7. (a) PUMA mesh adaptation, (b) VOF-to-DPM transition using WMLES S-Omega.

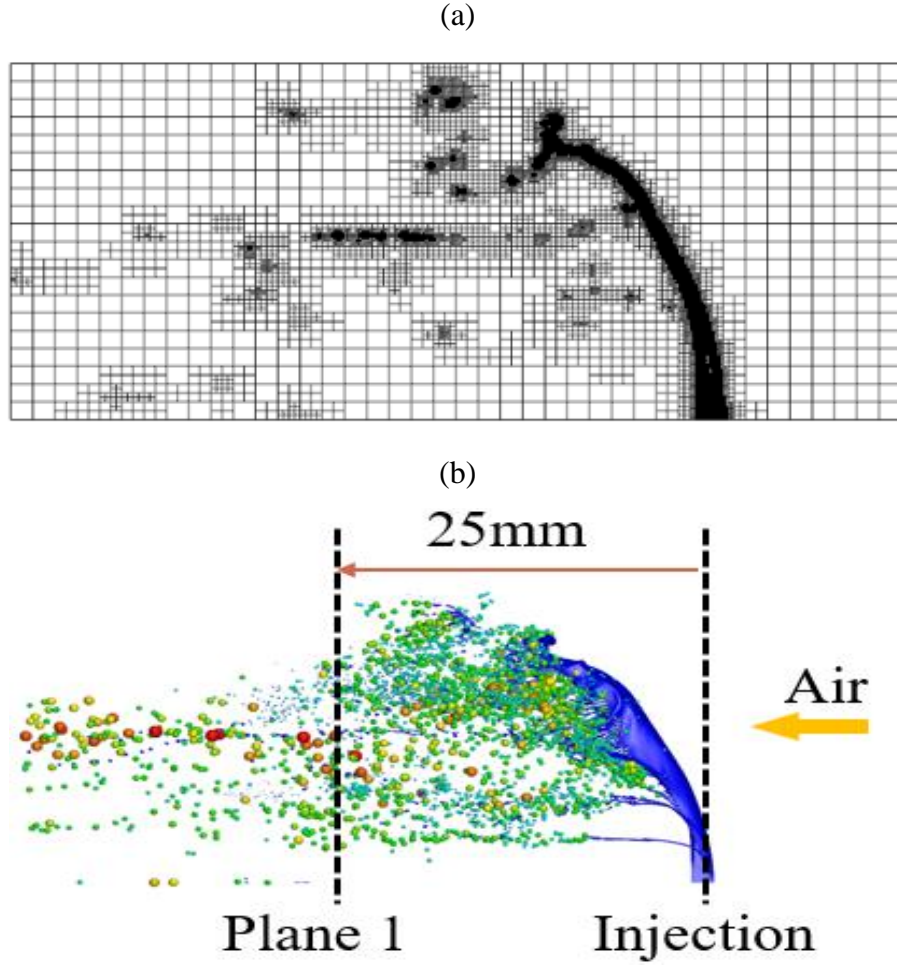


Figure 8. (a) Hanging Node Adaptation, (b) VOF-to-DPM transition using WMLES S-Omega.

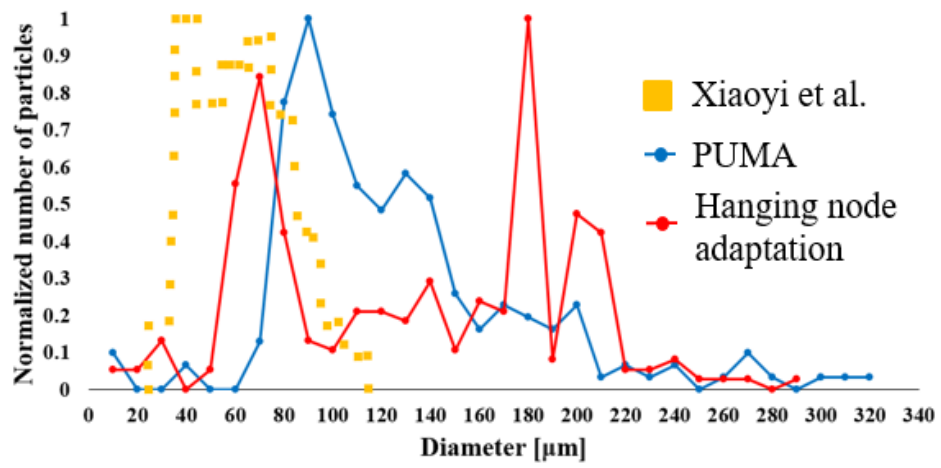


Figure 9. Effect of mesh adaptation methods in droplet size distribution on plane 1.

3.2.2 Effect of turbulence models

It was important to evaluate the accuracy of Large Eddy Simulations (LES) and Reynolds-Averaged Navier-Stokes (RANS) turbulence models by predicting results compared to Xiaoyi et al.'s work. Figure 10, Figure 11, and Figure 12 show the effect of turbulence models in the cross-section XY midplane. PUMA scheme was used for all three simulations. WMLES S-Omega was able to capture a large number of vortices in areas of flow separation, resulting in a higher resolution during the primary breakup of the liquid atomization. In contrast, Realizable k-epsilon and SST k-omega ignored oscillations, resulting in average flow distribution. Figure 13 indicates the droplet size distributions using three different turbulence models, SST k-omega model captures a wider size range.

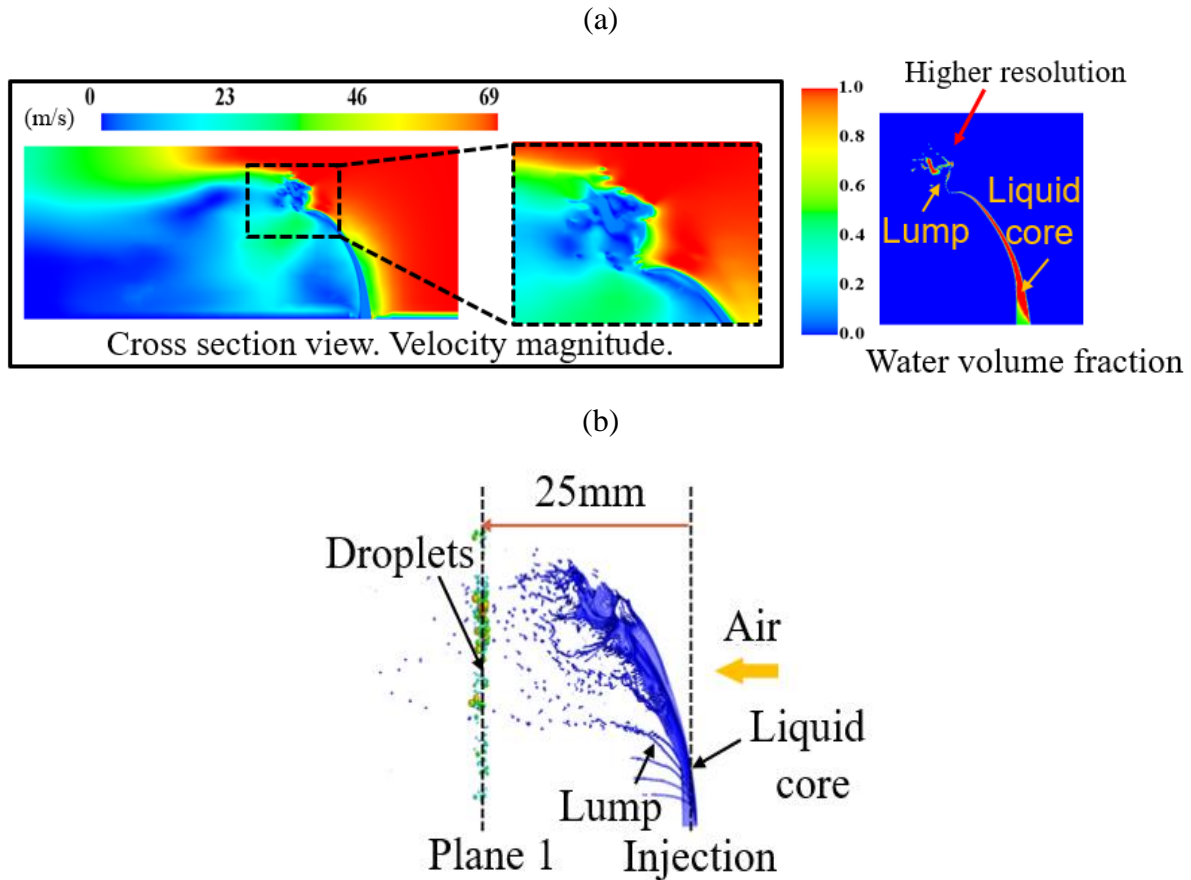


Figure 10. (a) Velocity and liquid volume fraction, (b) VOF-to-DPM transition using WMLES S-Omega.

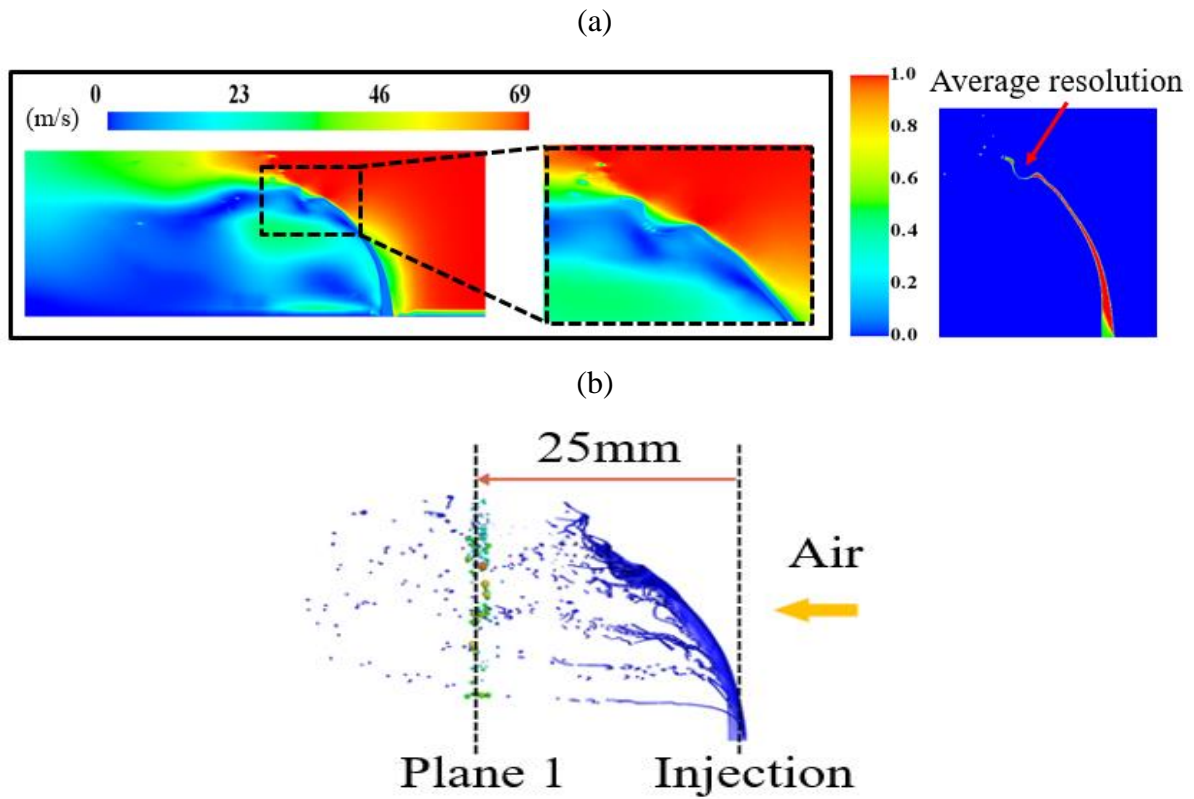


Figure 11. (a) Velocity and liquid volume fraction, (b) VOF-to-DPM transition using Realizable k-epsilon.

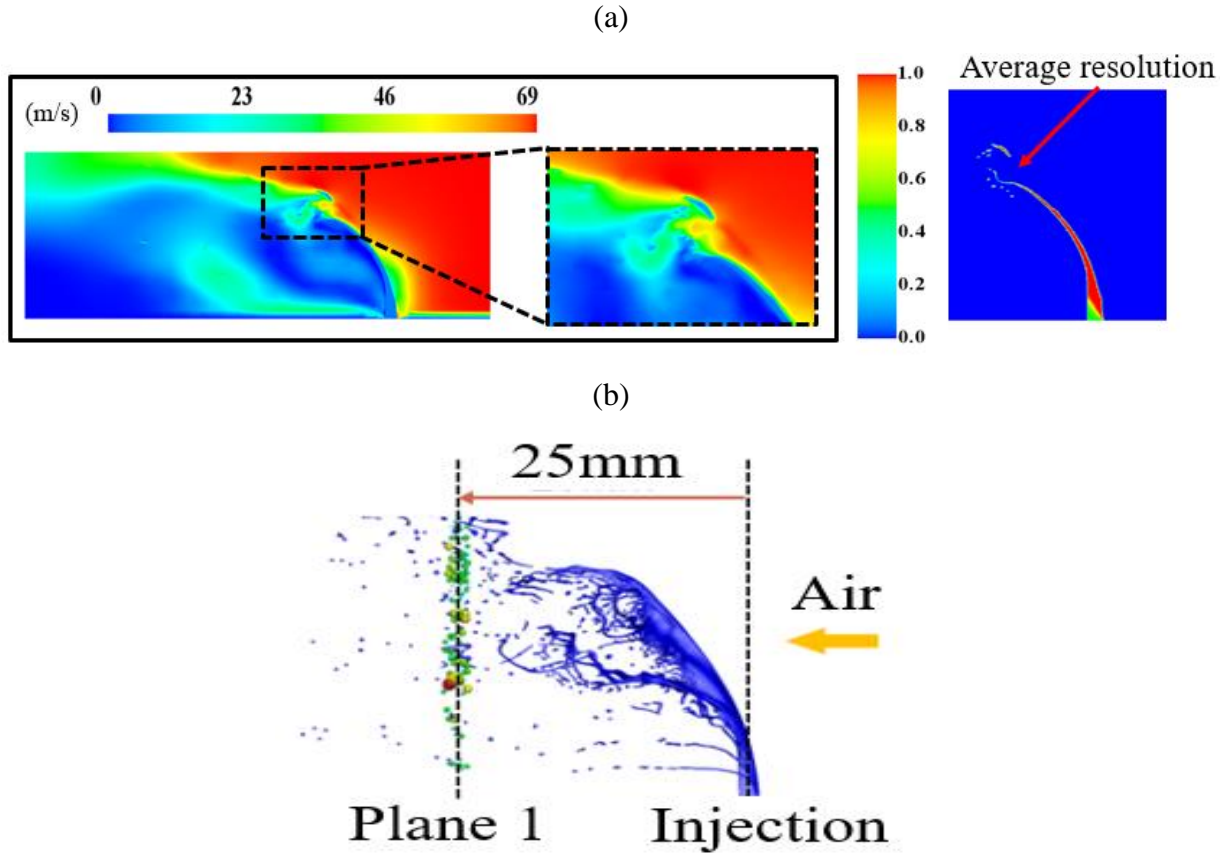


Figure 12. (a) Velocity and liquid volume fraction, (b) VOF-to-DPM using SST k-omega.

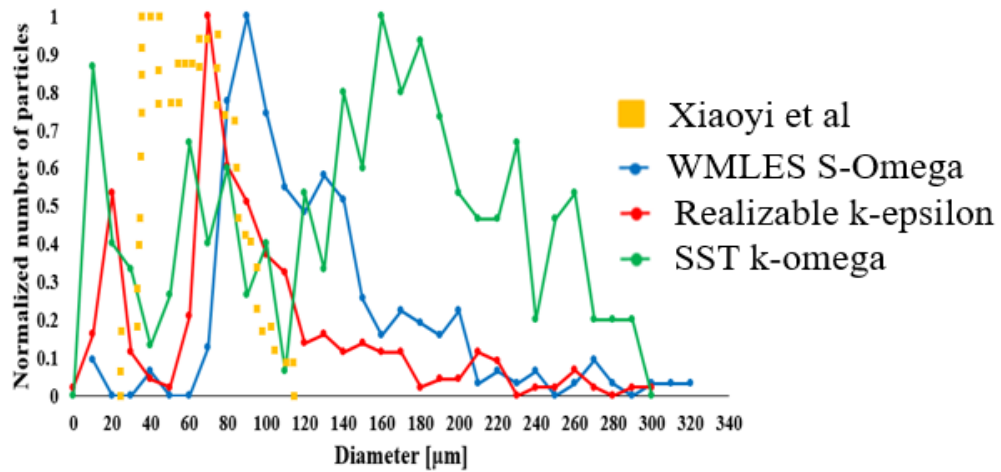


Figure 13. Effect of turbulence models in droplet size distribution on plane 1.

3.2.3 Effect of mesh resolution

A quantitative comparison of the total number of generated droplets based on mesh resolution can be seen in Table 4. PUMA and WMLES S-Omega turbulence model were used for all three mesh resolutions. This comparison gives an idea of the requirements for achieving a certain cell size where the VOF liquid phase after meeting the different transition criteria will be converted into DPM droplets. The finer the size, the more generated droplets can be analyzed. Considerations of using the VOF-to-DPM transition model are related to total mesh density, domain dimensions, other effects explained before, and computational running time since this model only works using Explicit scheme solver.

Table 4. Mesh resolution and total droplet generated.

Mesh resolution	Refinement levels	Cell size μm	Droplets #
41X21X21	5	50	2,700
128X64X64	4	25	13,100
128X64X64	5	12.5	49,900

3.3 Validation

These simulated results are compared to experimental data using Phase Doppler Particle Analyzer (PDPA) [28] and Xiaoyi et al.'s work [18]. The validation mesh from Figure 6 was used. Figure 14 illustrates the injection pattern after PUMA scheme takes effect after using 5 levels of refinements. A liquid film and ligaments breakup can be seen. The strong airstream at 69m/s velocity magnitude pushes downstream the liquid injection causing it to atomize, see Figure 15. WMLES S-Omega turbulence model was used to capture better the complicated aerodynamic behavior with higher resolution. The mesh will coarsen back up to the original cell

size when liquid droplets are generated. This can reduce the total cell number and computational time. Simulations were run to 1.686ms.

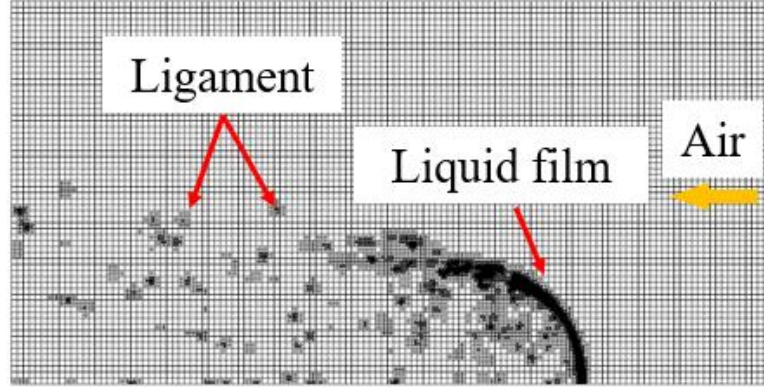


Figure 14. PUMA mesh adaptation on XY cross-section midplane.

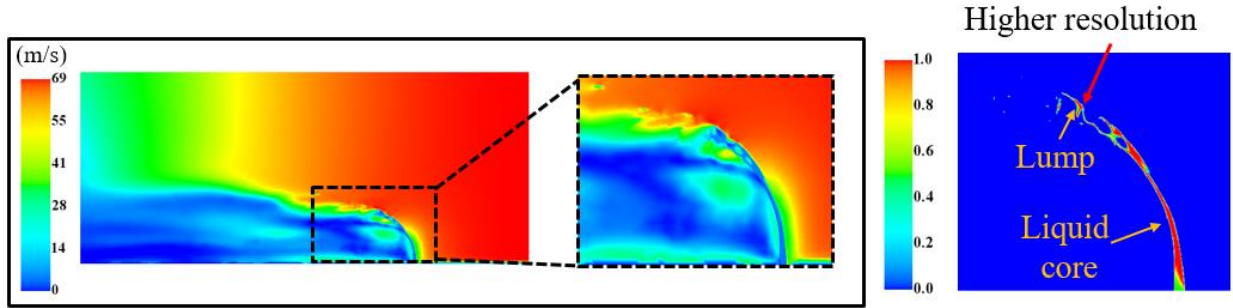


Figure 15. Velocity magnitude and liquid VOF.

The cross-flow simulation can share important insights in simulating a real air-mist nozzle process because the atomization process is obtained in both cases. That is why it is important to evaluate the feasibility to improve accuracy in convert liquid phase using the VOF model to liquid droplets using the DPM model. The VOF-to-DPM transition can be seen in Figure 16, the atomization process starts from liquid film and being pushed and distorted downstream because of air phase presence; as result, these distortions create liquid lumps or ligaments that later will be transformed to droplets. Figure 17 indicates two validations for simulated droplet size distribution. A sample of droplets was taken at a monitor plane located 25mm downstream of the liquid injection.

The first validation shows good prediction compared to the experiment when the maximum droplet diameter was set to $50\mu\text{m}$. The second validation also shows good size distribution compared to Xiaoyi et al.'s work when the maximum droplet diameter was set to $200\mu\text{m}$. The VOF-to-DPM transition model works better when an accurate input for minimum and maximum droplet size is specified as well as other considerations previously explained.

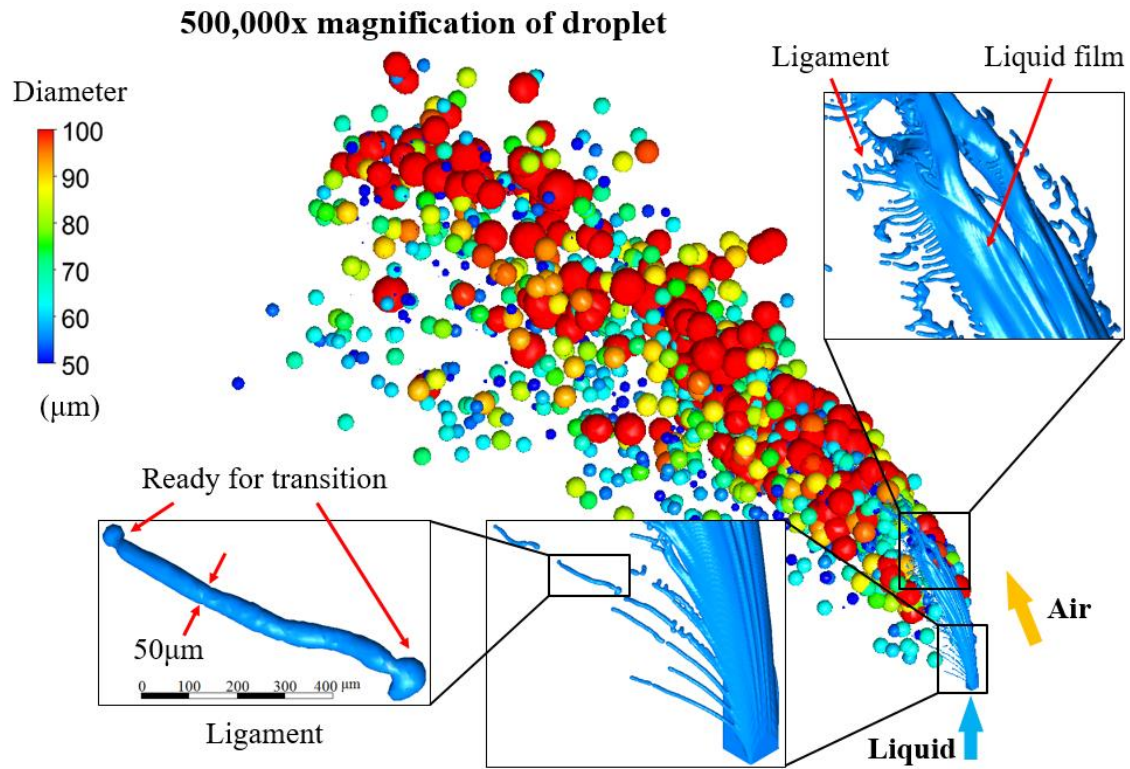


Figure 16. VOF-to-DPM transition.

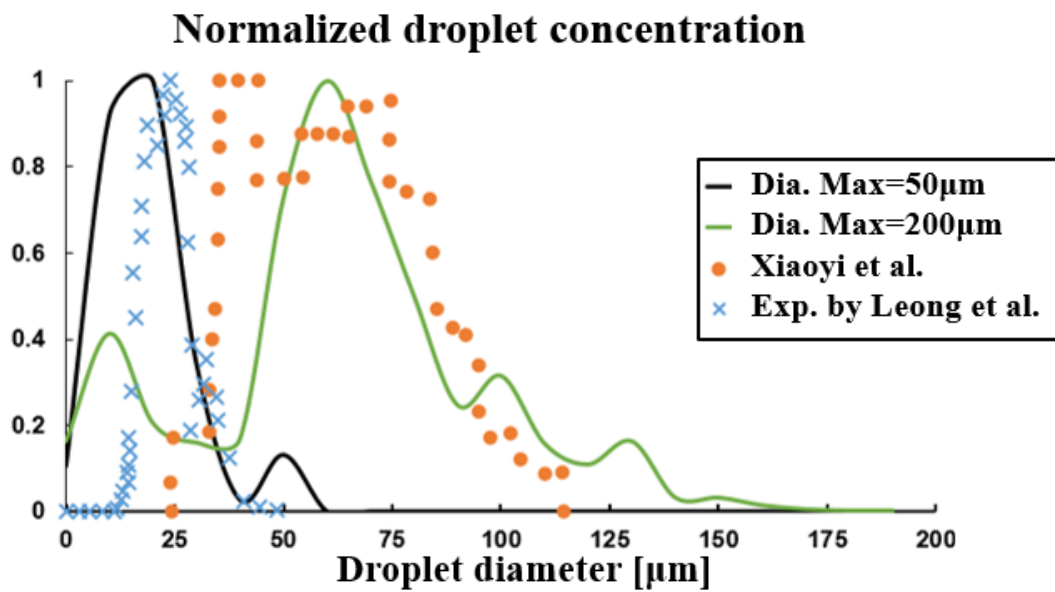


Figure 17. Validation for droplets size distribution.

CHAPTER 4. AIR-MIST NOZZLE SIMULATION

4.1 Nozzle internal region, Section 1 (VOF model)

4.1.1 Computational domain

A flat fan Delavan Cool-Cast W19917-15 air-mist nozzle was used to develop a methodology and conduct simulations in this research. The three-dimensional air-mist nozzle can be seen in Figure 18. Detailed dimensions and internal information are not be included in this research.

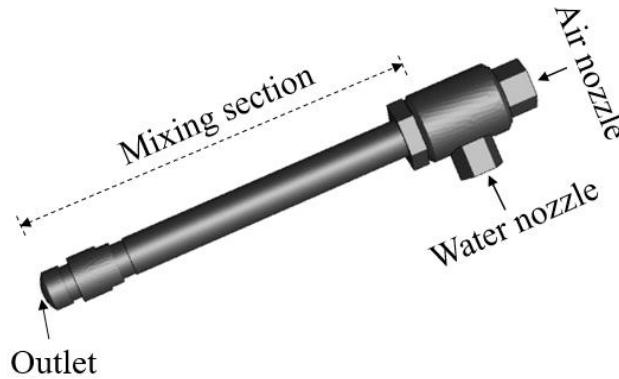


Figure 18. Section 1, Delavan Cool-Cast air-mist nozzle 3D geometry.

4.1.2 Boundary conditions and fluid-gas properties

Table 5 summaries all four simulation cases that were run according to the laboratory test report by Industrial collaborators. A pseudo automatic time step was used. Air as the primary phase while water as the secondary phase and Implicit VOF disperse interface scheme were used. Gravity was included in all cases. Water volumetric flow rates were converted from GPM to kg/s mass flow rates as 0.2837kg/s and 0.4101kg/s, from 4.5 GPM and 6.5 GPM respectively. Reynolds numbers for the water nozzle were calculated as 26658 and 38535, so k-omega SST was set for the turbulence model in order to calculate both inner and outer layers for internal flow.

Gas-liquid properties were interpolated based on operating conditions as explained in APPENDIX A. Constant gas-liquid properties were used during simulations. Surface tension of 0.0724 N/m was set. Water nozzle was set as mass flow inlet, air nozzle was set as pressure inlet, and nozzle tip outlet was set as pressure outlet at 1 atm.

Table 5. Boundary conditions for simulation cases.

Water inlet (psig / GPM)		Air inlet (psig)
60	4.5	30
60	4.5	40
95	6.5	30
95	6.5	40

4.1.3 Effect of mesh types and mesh sensitivity study

The study of mesh types was considered for section 1 of the air-mist nozzle process. Figure 19 compares the meshes using the tetrahedral type and polyhedral type. The tetrahedral mesh done in ANSYS Workbench shows that if the mesh transition along locations of interest e.g. water nozzle needs to be smooth, then an excessive cell number is obtained.

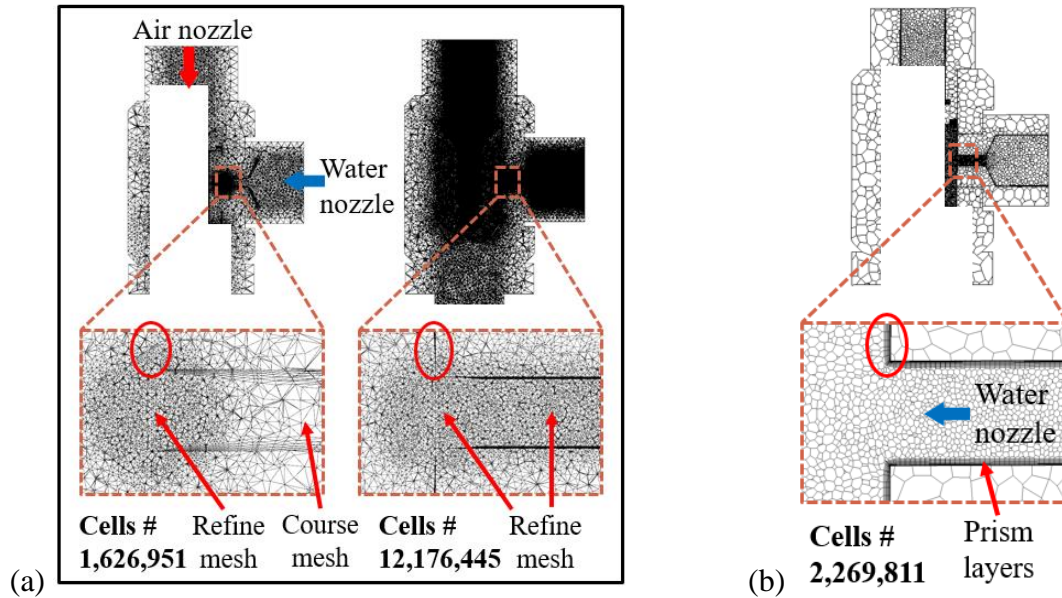


Figure 19. Tetrahedral mesh using ANSYS, (b) Polyhedral mesh using STAR-CCM+.

On the other hand, using polyhedral mesh done in STAR-CCM+ obtain a smooth transition with fewer cells number. A base size between 0.1mm to 1mm, a total number of 10 prism layers with a thickness of 0.2mm in order to capture flow characteristic close to the wall, and transition layers ratio of 1.1 was used for both meshes. Other advantages of using polyhedral mesh are conformal prism layers at corners and a better transition for VOF-to-DPM beyond the outlet nozzle tip because of the shape of a polyhedral cell. STAR-CCM+ 13.04.010 was only used to mesh the domain, ANSYS FLUENT 19.1 was used to run all simulations in section 1.

Therefore, polyhedral mesh type with prism layers was chosen to run simulations. A mesh sensitivity study was conducted using single-phase air with a constant velocity inlet of 1 m/s for both water and air inlets. Table 6 summaries the increments of cell number, meshing time, and quality. A surface remesher proximity technique was used to conduct local mesh refinement. Increment of cell number; thus, mesh time, were obtained by increasing this factor, and it happens as it was explained in CHAPTER 1. The quality percentage of the cell is improved by increasing this factor; however, all three cases had a quality percentage greater than 95% with wall y^+ below 2.2.

Table 6. Polyhedral mesh sensitivity study.

Surface remesher	Quality %	Cells #	Increment cells %	Mesh time [s]
2	95	376,836	0	90
10	97	908,387	141	174
20	98	2,269,811	502	455

Figure 20 illustrates the velocity for all three surface remesher factors along the internal reference line. Results for all factors do not differ much from each other, major difference can be seen at the beginning of the mixing section where factor 20 can potentially capture better the turbulence mixing. However, mesh resolution using factor 2 was used considering computational time.

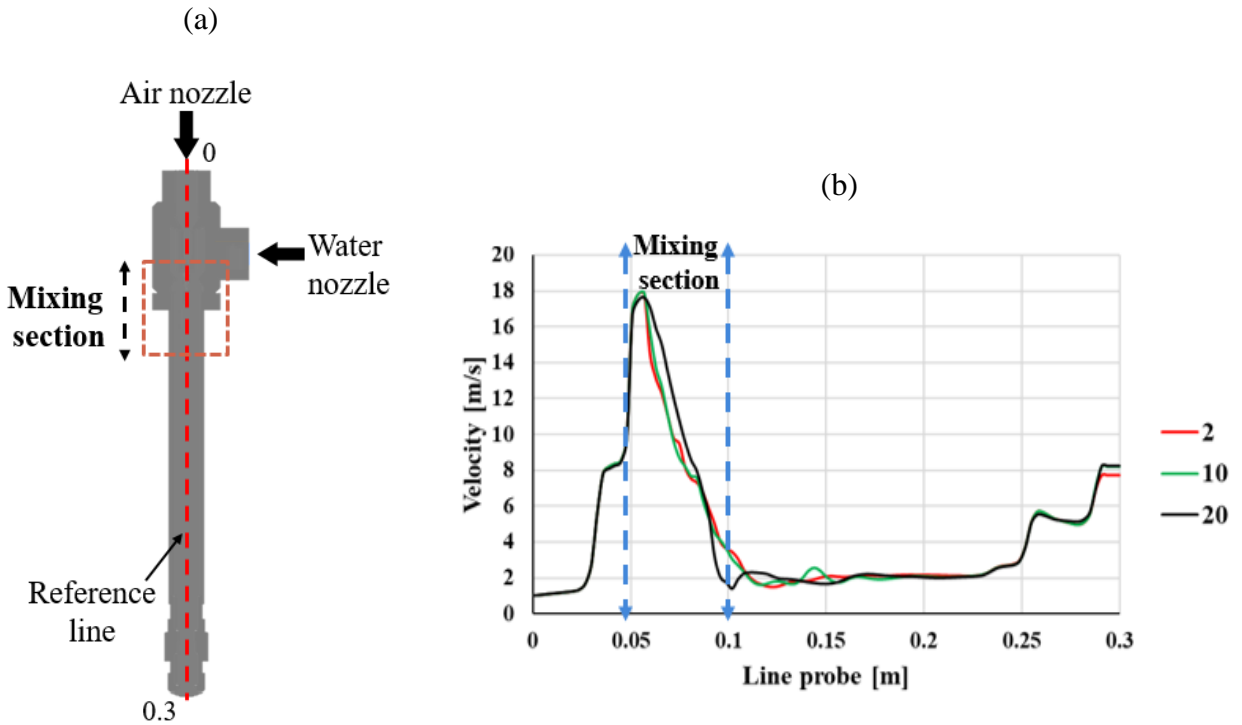


Figure 20. (a) Internal reference line (b) Velocity along the reference line for all surface remesher proximity factors.

4.1.4 Effect of operating conditions

Four cases were studied where the air pressure and water flow rate were variables. The CFD analysis was done using the internal reference line as seen in Figure 20. The absolute pressure can be seen in Figure 21 while Figure 22 shows the velocity magnitude and Figure 23 illustrates the water concentration VOF for all cases.

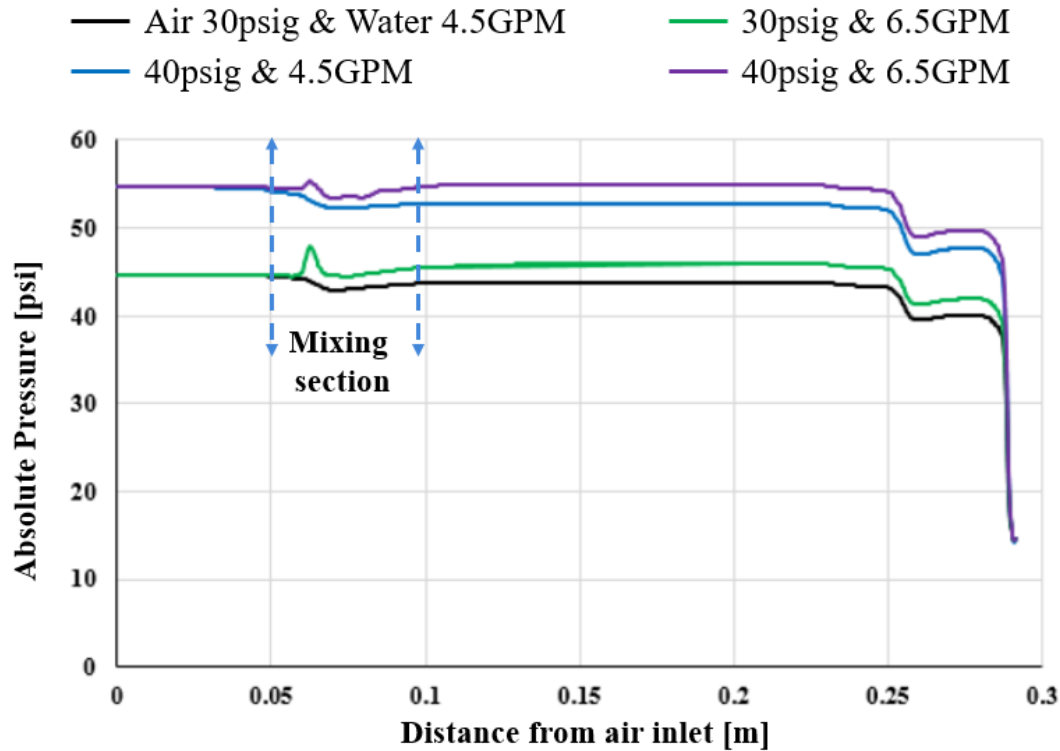


Figure 21. Absolute pressure along the reference line.

Increasing air pressure and maintaining fix the water flow rate reduces the water concentration inside the nozzle. Also, velocities inside the nozzle and at the outlet increase due to a larger pressure drop and the presence of the air phase. Increasing the water flow rate and maintaining fix the air pressure increases the water concentration in the nozzle as expected. Also, velocities inside the nozzle and at the outlet decrease due to the larger presence of the water phase. Some major differences in the flow were seen at the start of the mixing section.

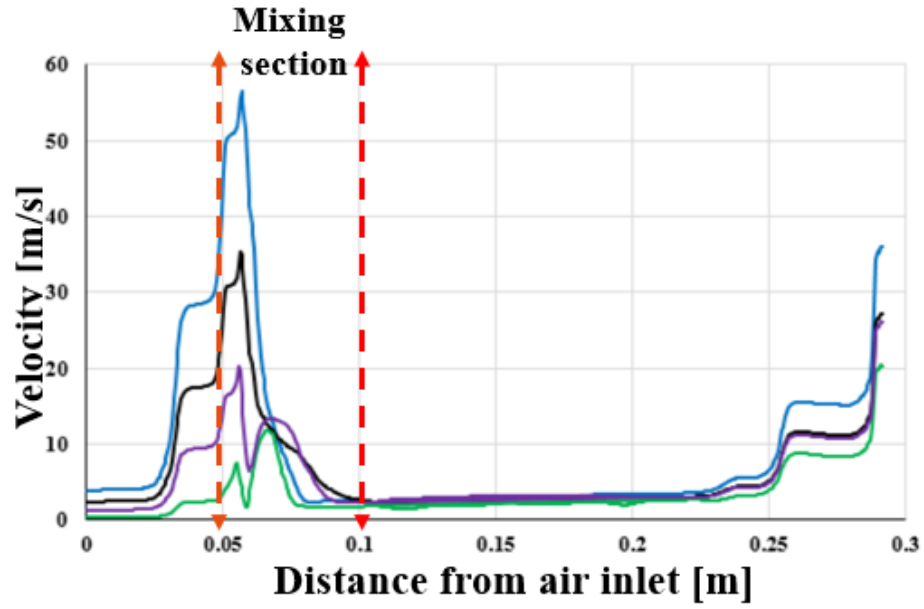


Figure 22. Velocity magnitude along the reference line.

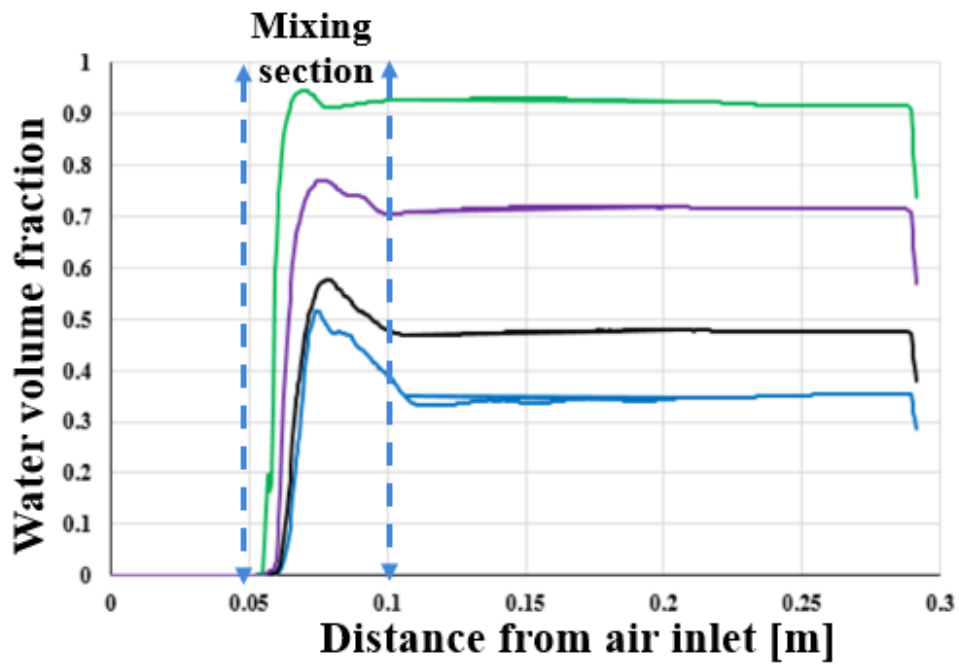


Figure 23. Water concentration VOF along the reference line.

Conditions close to the outlet nozzle tip will be used as the inlet conditions for the external spray simulations for Section 2, see Table 7.

Table 7. Conditions at the nozzle tip.

Cases (psig and GPM)	CFD Simulation	
	Water fraction (Nozzle tip)	Velocity mag. (m/s) (Nozzle tip)
30 and 4.5	0.38	27.16
40 and 4.5	0.28	35.94
30 and 6.5	0.74	20.35
40 and 6.5	0.57	26.08

4.1.5 Quasi-steady state of simulation cases

A probe point was located close to the nozzle outlet tip in order to check when the solution reached to quasi-steady state, see Figure 24. A pseudo automatic time step was used, and all simulation cases start converging at 10,000 iterations, yet 20,000 iterations was chosen as benchmark for future simulations, see Figure 25.

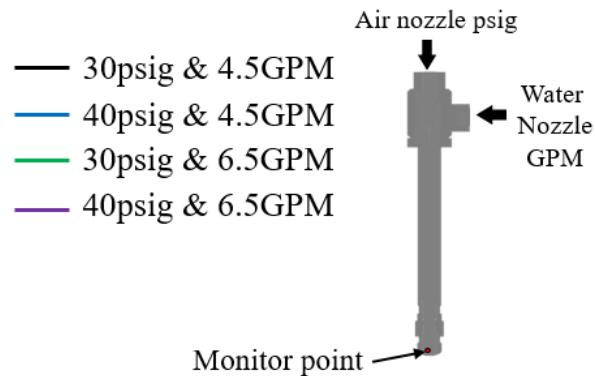


Figure 24. Monitor point.

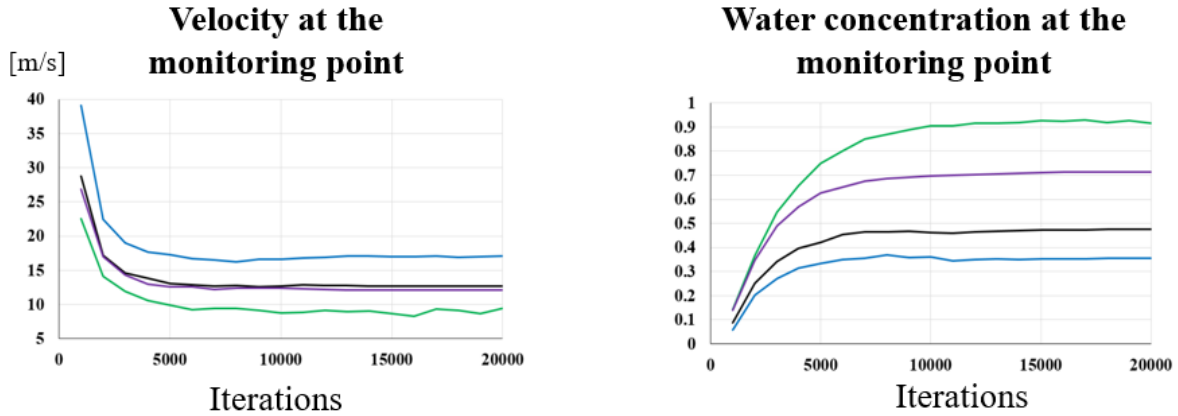


Figure 25. The convergence of the probe point at 20,000 iterations.

4.2 Spray formation region, Section 2

4.2.1 Computational domain and boundary conditions

Air domain dimensions are determined based on measurement distance during the test by Industrial collaborators, and the flat fan air-mist spray characterization, see Figure 26. Different mesh resolutions were used in this section, depending on the goal that will be explained accordingly. STAR-CCM+ 13.04.010 was used to mesh the domain, ANSYS FLUENT 19.1 was used to run simulations in section 2 using VOF-to-DPM transition model. Nukiyama-Tanasawa distribution equation model was run using STAR-CCM+ 13.04.010.

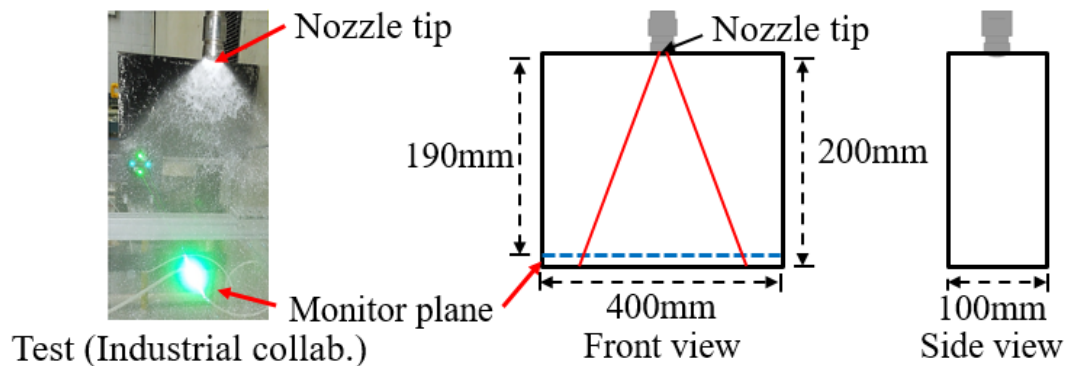


Figure 26. Section 2, spray region.

Figure 27 shows a polyhedral mesh with a refined potential core area, where the cell size is $500\mu\text{m}$. Potential core length is 40mm downstream of the nozzle tip compared to the test and Zhang's experimental results published 40-80mm potential core length [9] . The refined was achieved using wake refinement with a spread angle of 28° . The rest of the cell size are 3mm with a growth factor of 1. Polyhedral type mesh was chosen because of the shape of a polyhedral cell in order to have a better transition for VOF-to-DPM. However, this mesh will only be used to develop the flow pattern using the VOF model.

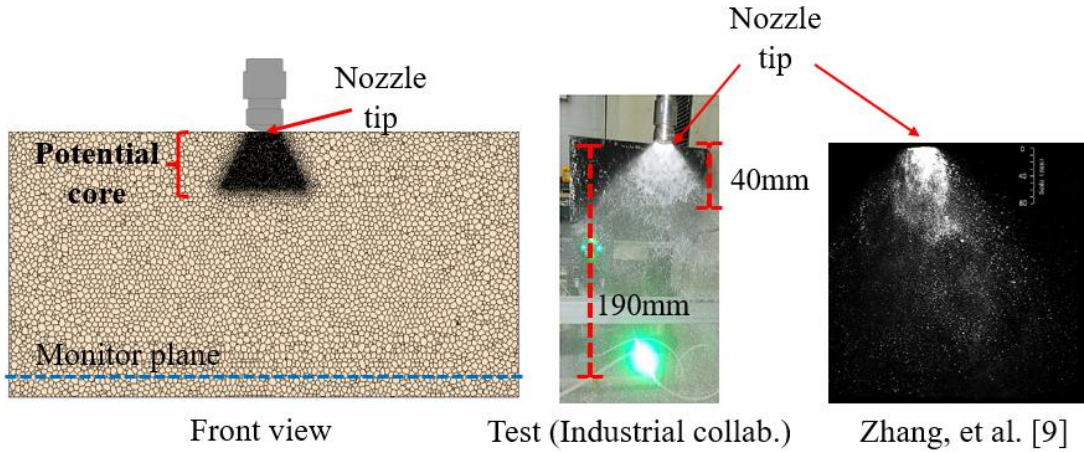


Figure 27. Polyhedral mesh, potential core area refined ($500\mu\text{m}$).

Mesh resolution in Figure 28 has finer refinement at the potential core, $100\mu\text{m}$ cell size. In order for the VOF-to-DPM transition model to be effective and produce accurate results, the cell size needs to be close to the droplet size which is in orders of microns. No mesh adaptation was used because having already a total of 7.5 million cells. The rest of the cell size are 6mm with a growth factor of 3. No wake refinement was used for the potential core area in order to reduce the number of cells, instead, an imprinted shape with a close dispersion angle for the flat fan air-mist nozzle was used. Boundary conditions for both meshes using polyhedral are the top injection imprinted face close to the dimensions at the reference location was set as velocity inlet with profile from section 1 with velocity components and water volume fraction. The rest of the top surface was set to pressure outlet as well as the other faces of the air domain.

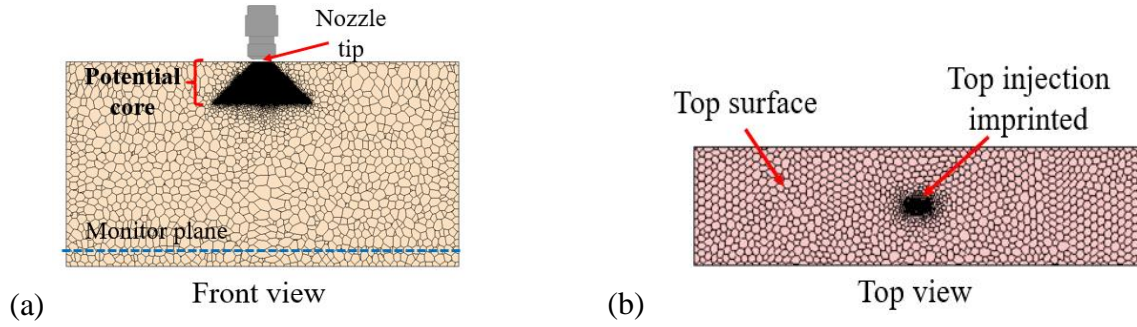


Figure 28. (a) Potential core area refined (100 μ m), (b) Top view injection imprinted face.

A hexahedral mesh type was used to simulate water droplets using Nukiyama-Tanasawa distribution equation model, see Figure 29. This model assumes no transition from water ligaments to water droplets, so the domain was considered after the potential core. A total of 0.25 million cells was obtained after cell size varies from 1mm in the top injection imprinted face and the rest of the domain with cells size of 3mm. Boundary conditions for this mesh are the whole top surface as velocity inlet mapping the profile after the flow has been developed in section 2 using mesh from Figure 27, all other surfaces as pressure outlet. Gravity and k-omega SST turbulence model were used for all meshes discussed. Also, fluid-gas properties are referred to as atmospheric conditions.

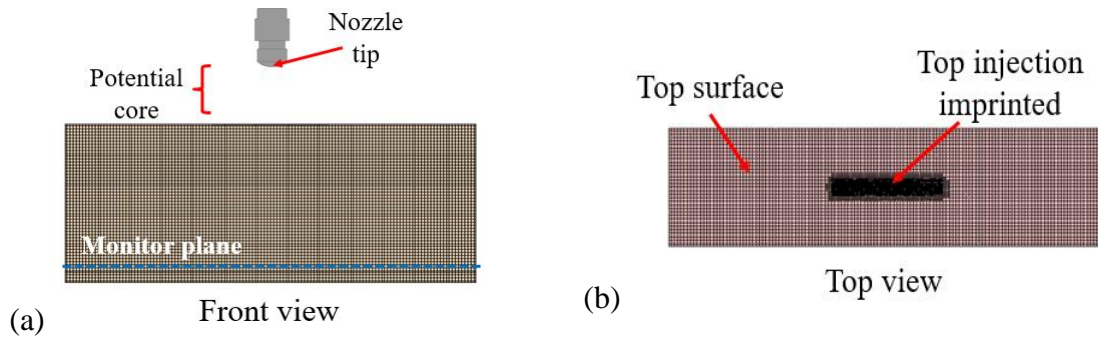


Figure 29. (a) Hexahedral mesh, (b) top view injection imprinted face (1mm).

4.2.2 Spray characterization (VOF model)

Section 1 can be linked with section 2 as explained before in the methodology section by creating a horizontal cut plane close to the nozzle tip. This plane named top injection imprinted will contain velocity coordinates and volume fractions for both phases in section 1. Using mesh from Figure 27, a new isothermal transient simulation with a time step of 1×10^{-3} seconds was run. Implicit VOF-Compressive sharp interface scheme was used. Velocity boundary conditions were set by using the plane profiles for all the four cases. As a result, Figure 30 shows the air-mist nozzle spray characterization for all cases. The condition using 4.5GPM and 30psig shows a similar velocity magnitude than using 6.5GPM and 40psig. The highest velocity magnitude is obtained using 4.5GPM and 40psig, while the lowest velocity magnitude is obtained using 6.5GPM and 30psig.

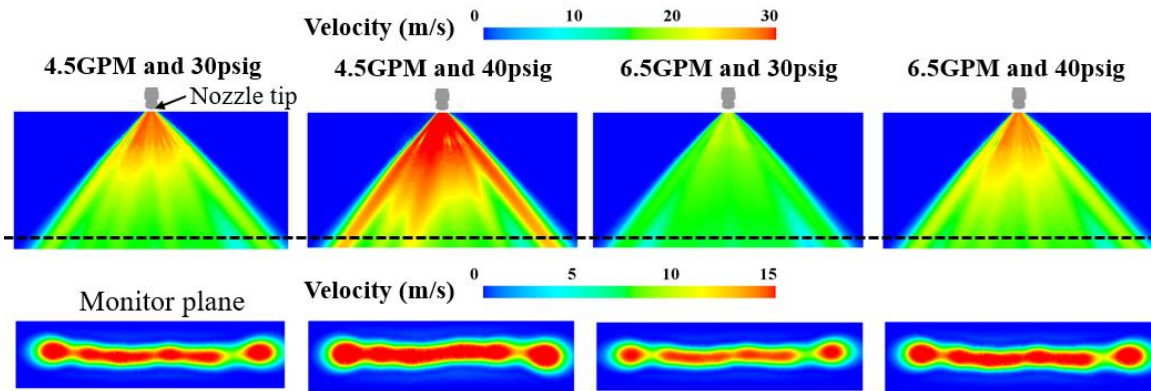


Figure 30. Air-mist nozzles spray characterization.

Figure 31 illustrates the simulated result against the test by Industrial collaborators showing similarities such as a higher accumulation of water close to the nozzle tip being represented by 10% of the water phase. Also, the air phase presence is strong in simulating an air-mist nozzle. Droplets should start appearing from the breakup process from the potential core also identified as the primary breakup region, this will cause the water concentration in the continuous to decrease. It is recommended that the flow velocity and VOF phases are developed before droplets start generating. That is why the importance of the current work being discusses.

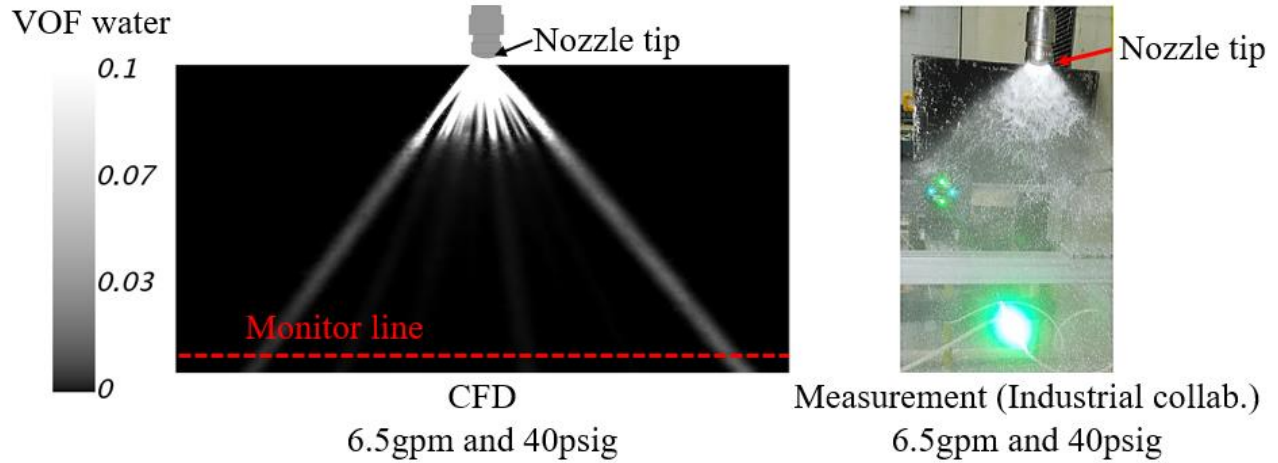


Figure 31. CFD and test spray comparison.

Table 8 summarizes relations of operating conditions and velocity for all cases compared to measurements. For example, it can be stated that if air pressure is increase, then the velocity of droplet is increase. On the other hand, if the water flow rate is increase, then the velocity of droplet is decrease. Even though this comparison should be done against droplets which at this stage of simulation, there are none, the comparison is done against injected VOF phases and velocity profiles. These relations also agree with findings published in [10] . Injected profiles will have a strong influence in droplets trajectory and velocity.

Table 8. Relations of operating conditions and velocity of the air-mist nozzle.

Measurement (Industrial collab.)		CFD Simulation	
Condition (GPM & psig)	Avr. droplet velocity (m/s)	Velocity (m/s) (Nozzle tip)	Water VOF (Nozzle tip)
4.5 & 30	17	27.16	0.38
4.5 & 40	22	35.94	0.28
6.5 & 30	14	20.35	0.74
6.5 & 40	17	26.08	0.57

A midline at the same monitor reference location as the test across the front view was used to collect velocity simulated data. Table 9 compares the measurement results for all conditions with CFD spray characterization simulations, showing similar results among them. Let's remember the continuous flow will have a strong influence in droplets; thus, it was important to simulate the flow characterization before generating droplets.

Table 9. Comparison measurement and CFD continuous at monitor location

Measurement at monitor location (Industrial collab.)		CFD Simulation at monitor location	
Condition (GPM and psig)	Avr. droplet velocity (m/s)	Max. velocity (m/s)	Avr. velocity (m/s)
4.5 and 30	17	18.5	17
4.5 and 40	22	23.5	21.5
6.5 and 30	14	15	13
6.5 and 40	17	19	17

4.2.3 Droplet generation methods

Two methods to generate water droplets were proposed in CHAPTER 2.

4.2.3.1 VOF-to-DPM model

The flow developed during the spray characterization will serve as initial conditions to use the VOF-to-DPM transition model but using mesh from Figure 28. A new isothermal explicit transient simulation with a time step of 1×10^{-5} seconds was set. VOF-Geo-Reconstruct sharp interface scheme was used. Stochastic collision, wave breakup, and one-way coupling between DPM and continuous phase were added. A minimum and maximum droplet size of 0 and – 1mm

was set. A value of 0.5 for both radius standard deviation and radius-surface orthogonality and a split parcel factor of 25 were set.

4.2.3.2 Nukiyama-Tanasawa distribution equation model (DPM model)

Figure 32 shows a typical droplet size distribution that was extrapolated from [5] using WebPlotDigitizer. Nukiyama-Tanasawa distribution equation needs to specify the minimum, maximum, and mean droplet size. A complete data was not reported from the experiment. Thus, a ratio, which can accurately approximate the limits for size distribution based on operating conditions, was found by relating known limits found in [5] and available data from the experiment.

Comparison of nominal values from experiment and prediction using the ratio can be seen in APPENDIX B. The ratio works and it will always create the cumulative volume size distribution. If a size distribution for a new operating condition needs limits, then interpolation between two known ratios could be done, and use that ratio to approximate newer limits based on the operating conditions. All the blank spaces in Figure B. 1 are because they were not reported and therefore cannot be compared.

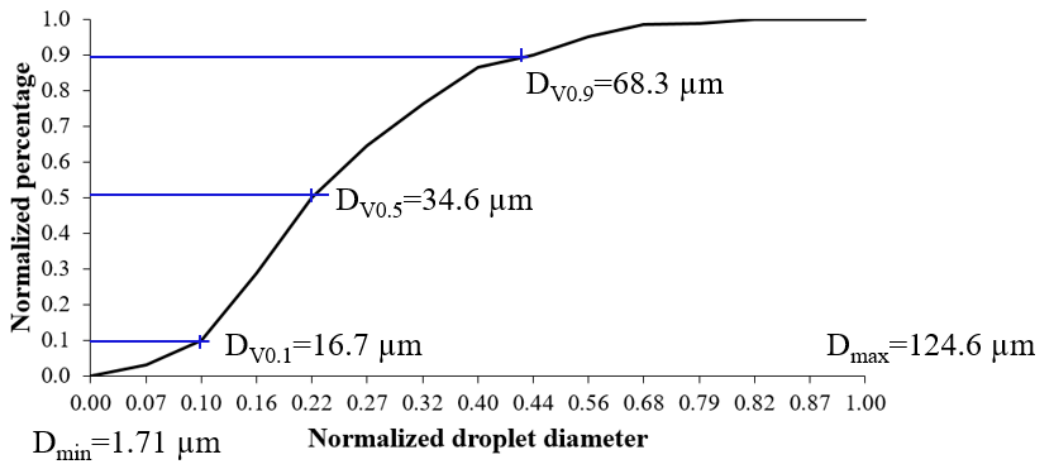


Figure 32. Normalized typical cumulative volume size distribution [5] .

Nukiyama-Tanasawa function distribution needs two specify two more constants, alpha with a value of 2 and beta with a value of 1. Velocity coordinates from the developed flow as seen in Figure 30 was set up in the imprinted surface injector. A time step of 1×10^{-3} seconds was used. Implicit solver and similar models for DPM and continuous were set. The mesh from Figure 29 was used for this simulation.

4.3 Validation

A complete spray simulation can be seen in Figure 33. Only one operating condition was chosen for validating. Air pressure 30psig and water flow rate 4.5GPM. A side by side comparison is shown in Figure 34. VOF-to-DPM transition model successfully works generating droplets up to $1000\mu\text{m}$. Mesh in some regions in the air domain is still considered coarse, then bigger droplets will be generated, falling off the expected size range. On the other hand, Nukiyama-Tanasawa produces a much more uniform droplet distribution. Droplets comparison were done at 0.55 seconds.

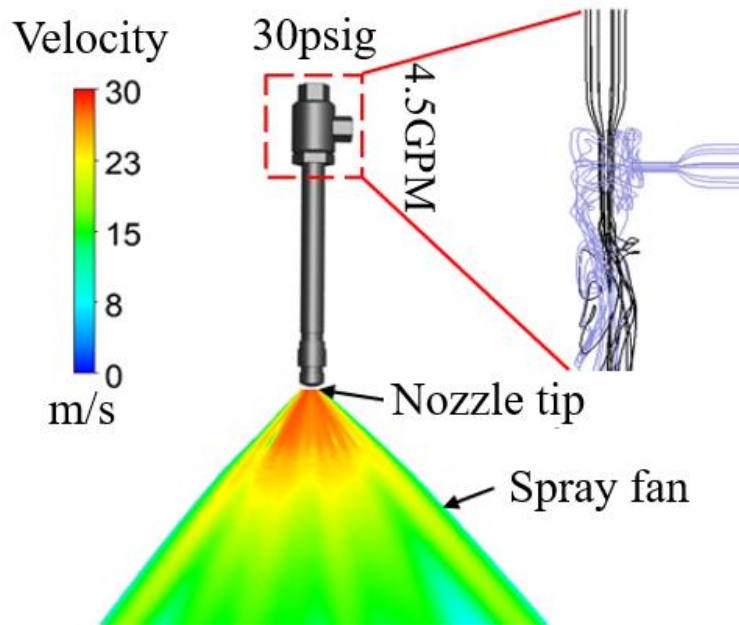


Figure 33. Air-mist spray velocity magnitude.

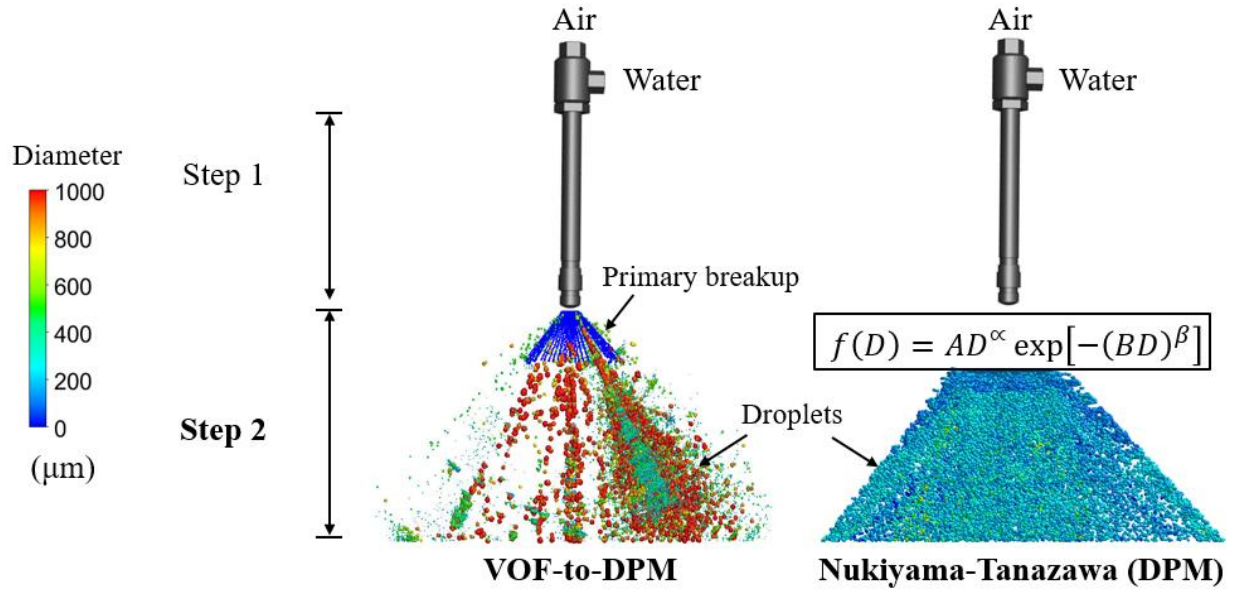


Figure 34. Comparison of droplet generation methods.

Table 10 summarizes the performance of both droplet generation methods. VOF-to-DPM transition uses Explicit solver meaning that the time step needs to be accordingly adjusted to improve conservation. This method requires a high-resolution mesh increasing mesh density and computational time. Instead, Nukiyama-Tanasawa distribution equation uses Implicit solver, less mesh, and fast running time.

Table 10. Performance of droplet generation methods.

Approach	VOF-to-DPM	Nukiyama-Tanazawa (DPM)
Solver	Explicit ($\Delta t=1 \times 10^{-5}$ sec)	Implicit ($\Delta t=1 \times 10^{-3}$ sec)
Running time (40 cores)	60 hr	1 hr
Mesh	7.5M	0.25M
Number of droplets	Fewer	More

Simulated droplets measurements were taken on the same monitor plane as the test, about 190mm from the nozzle tip. Results for cumulative droplet size distribution plot for both methods can be seen in Figure 35. Validation shows that Nukiyama-Tanasawa produces less percentage difference against test data for droplet size and droplet velocity magnitude. Both methods can be used to predict droplet aerodynamics behavior.

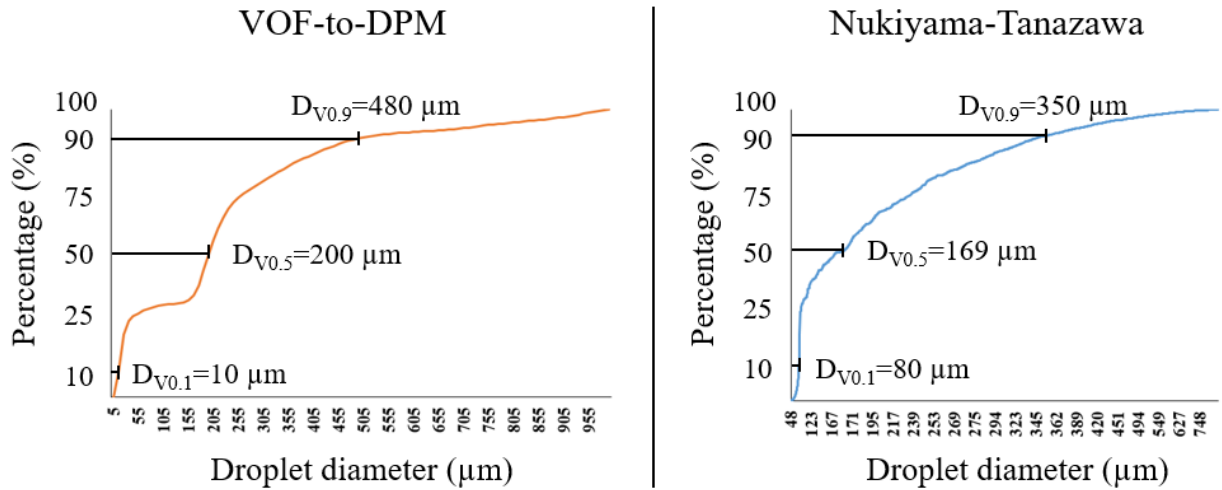


Figure 35. Cumulative volume size distribution for both methods.

Table 11. Validation for droplet size distribution.

	$D_{V0.1}(\mu\text{m})$	$D_{V0.5}(\mu\text{m})$	$D_{V0.9}(\mu\text{m})$	Velocity (m/s)
Test. (Industrial collab.)	75	170	324	17
VOF-to-DPM	10 (86.7%)	200 (17.6%)	480 (48.1%)	20.4 (20%)
Nukiyama-Tanasawa	80 (6.7%)	169 (0.6%)	350 (8.0%)	13.9 (18.2%)

CHAPTER 5. AIR-MIST NOZZLES COMPARISON

5.1 Nozzle internal region, Section 1 (VOF model)

5.1.1 Computational domain and boundary conditions

A second flat fan air-mist nozzle is being simulated, see Figure 36. This air-mist nozzle is 35% smaller compared to the air-mist nozzle in Figure 18, considering the overall length. Details for internal dimensions will not be discussed. Water pressure of 60psig or its equivalent flow rate of 4.5GPM and air pressure of 30psig were used as the operating condition. Same CFD models and gas-liquid properties based on the corresponding operating condition as explain before in CHAPTER 4 were used. The goal of this chapter is to use the developed methodology in other types of air-mist nozzles and compared them.

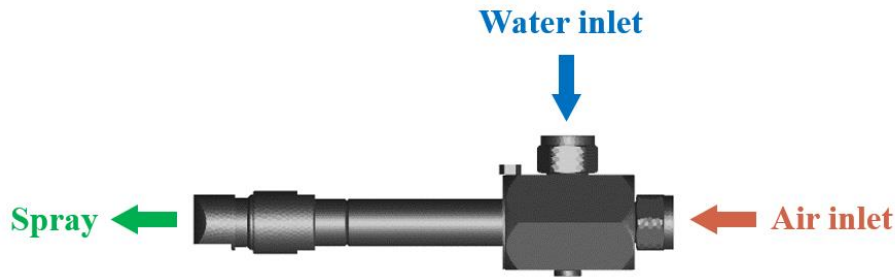


Figure 36. Section 1, Spraying System Caster-Jet 3D model.

5.1.2 Mesh sensitivity study

The same mesh type and settings as stated in CHAPTER 4 were used. A mesh sensitivity study was done using single-phase air with a constant velocity inlet of 1 m/s for both water and air inlets. Table 12 shows the increments of cell number, meshing time, and quality as the surface remesher proximity factor increases. The quality percentage of the cell is improved by increasing this factor with quality greater than 97% with wall y^+ below 7.

Table 12. Polyhedral mesh sensitivity study.

Surface remesher	Quality %	Cells #	Increment cells %	Mesh time [s]
2	97	489,244	0	100
10	97.3	734,828	50	120
20	98	1,517,221	210	201

Figure 37 shows the velocity for all three surface remesher factors along the internal reference line. The major difference between all three cases can be seen at the beginning of the mixing section where factor 20 could potentially capture better the turbulence mixing with an increment in computational time. A mesh resolution using factor 10 was used to conduct the simulation for this air-mist nozzle in section 1.

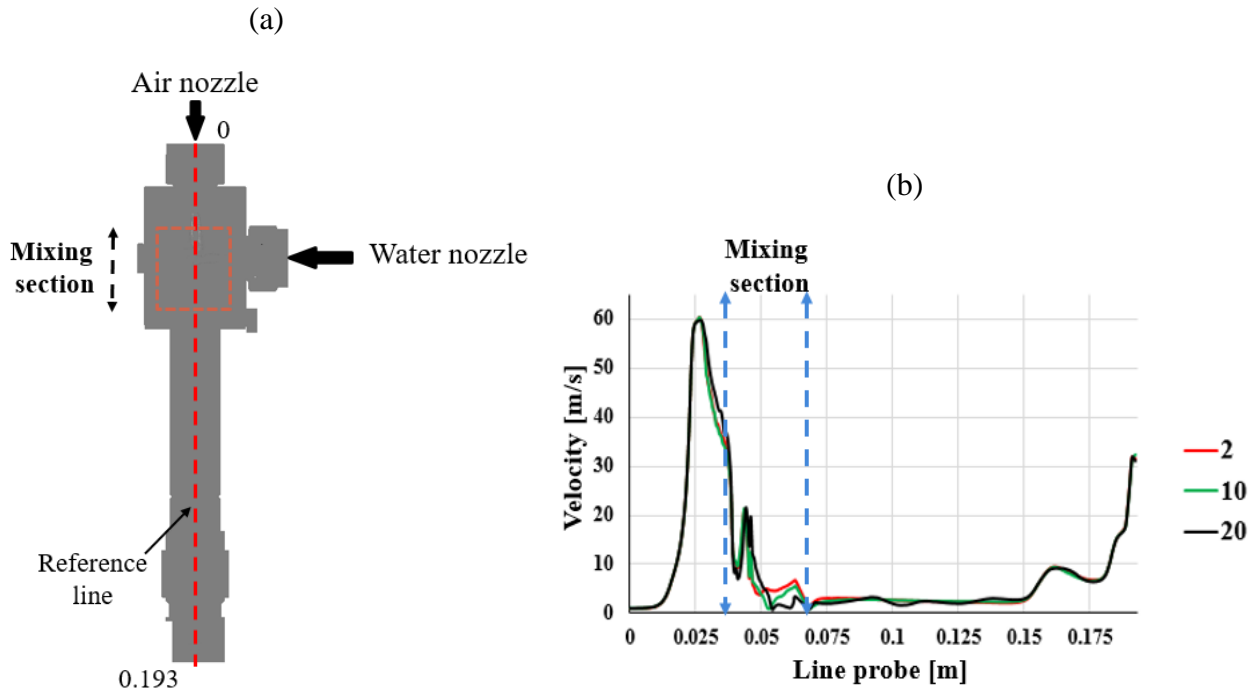


Figure 37. (a) Internal reference line, (b) Velocity along the reference line for all surface remesher proximity factors.

5.1.3 Air-mist nozzles comparison

The internal reference line as seen in Figure 37 was used for the CFD analysis. The absolute pressure can be seen in Figure 38 while the velocity magnitude in Figure 39 and the water concentration VOF in Figure 40. Major differences for each type nozzle can be seen at the start of their mixing section, and that is because each has a specific internal design.

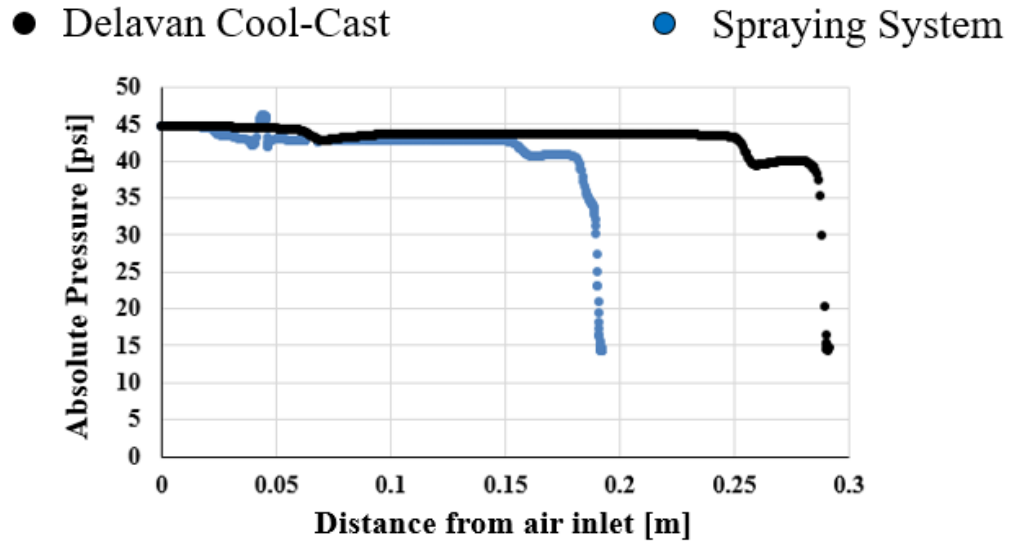


Figure 38. Absolute pressure along the reference line.

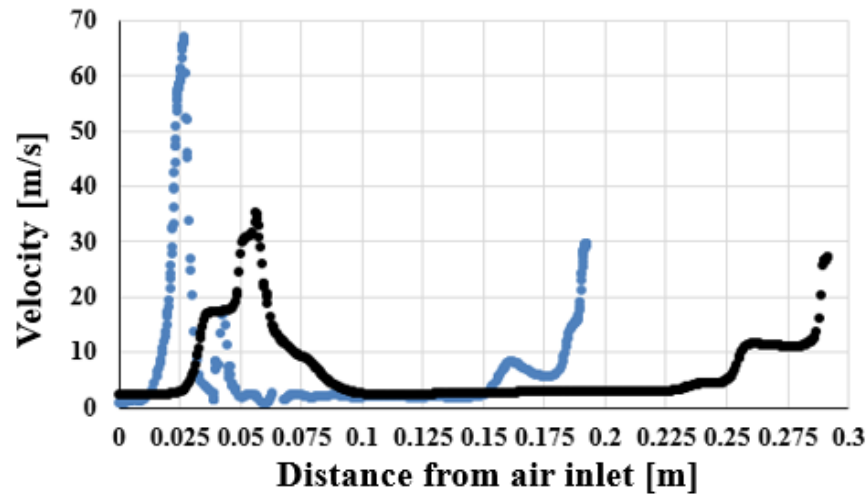


Figure 39. Velocity magnitude along the reference line.

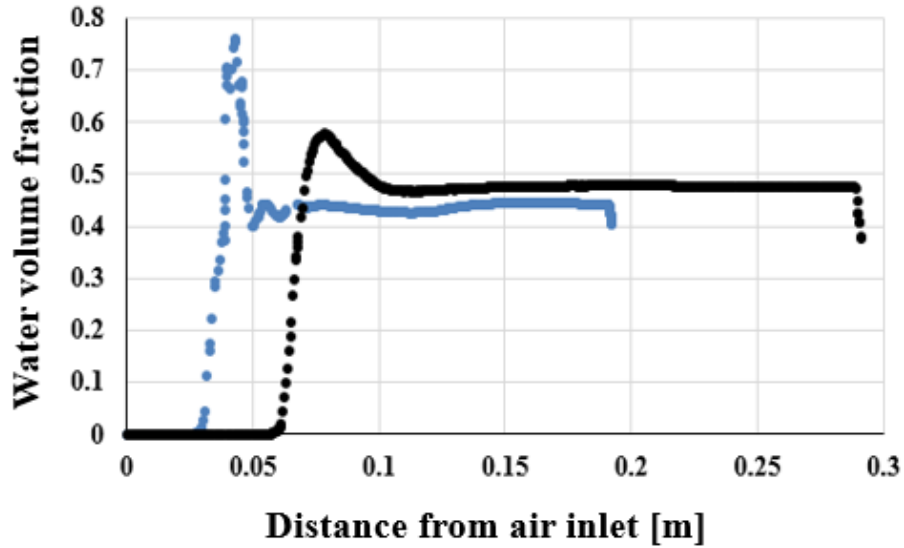


Figure 40. Water concentration VOF along the reference line.

Both nozzles show similar performance at the nozzle tip outlet, this can be due to the fact that the same boundary condition is set for both simulations, see Table 13. Spraying System nozzle shows an 8.5 percent difference in velocity increase, this can improve the droplet breakup.

Table 13. Conditions at the nozzle tip.

Nozzle type	CFD Simulation	
	Water concentration (Nozzle tip)	Velocity (m/s) (Nozzle tip)
Delavan	0.38	27.16
Spraying System	0.4	29.46

5.1.4 Quasi-steady state of simulation cases

Monitor probe points close to nozzles tip checked when the solution reached to quasi-steady state as seen in Figure 41. A pseudo automatic time step and Implicit VOF disperse interface scheme

allow the simulation cases to reach quasi-steady conditions at 20,000 iterations, see Figure 42. Velocity and water VOF conditions have converged and will serve as inlet conditions for the external spray simulations for Section 2.

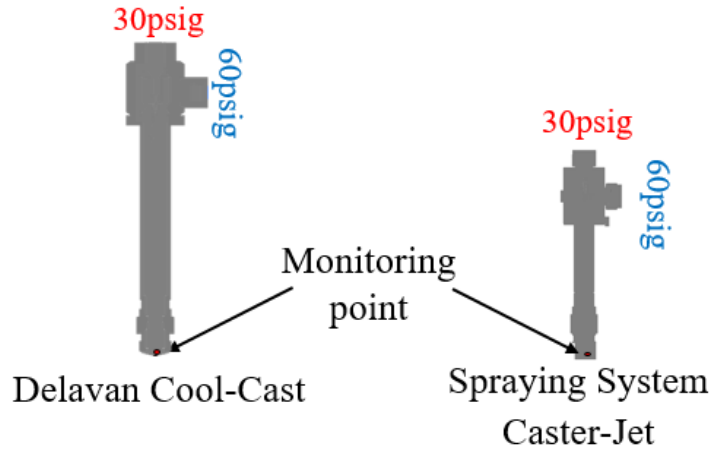


Figure 41. Monitor points.

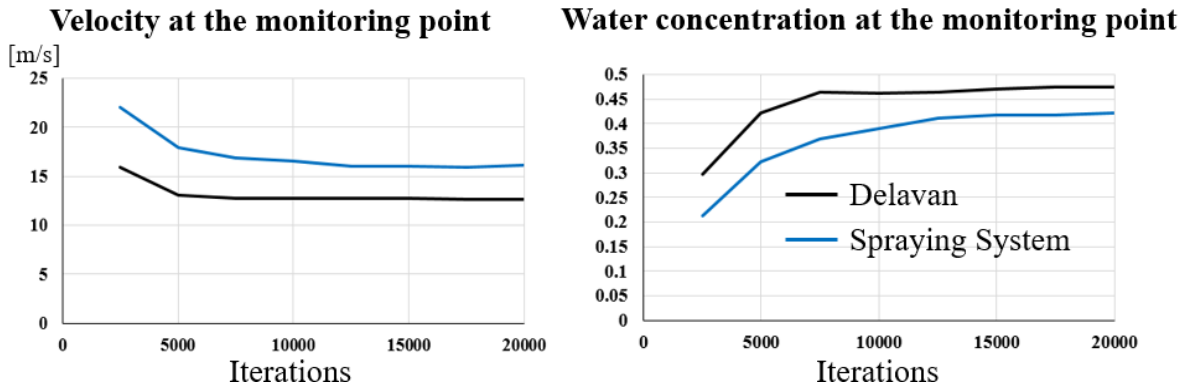


Figure 42. The convergence of the probe point at 20,000 iterations.

5.2 Spray characterization between nozzles, Section 2 (VOF model)

The continuous flow needs to be developed before conducting DPM analysis. For computational domain, mesh resolution, simulation settings, and boundary conditions for this simulation refer to CHAPTER 4. The only difference is to update in the plane profile named top injection imprinted with the simulation results from section 1 using Spraying System nozzle. If plane profile dimensions change based on internal design, then a new mesh needs to be done using

similar cell sizes as explained before. Figure 43 shows the air-mist nozzles spray characterization. Streamlines illustrate the internal interaction of fluid-gas. Delavan air-mist nozzle produces a wider spray and also the primary breakup represented by creating an isosurface with water VOF of 0.05 is bigger compared to Spraying System air-mist nozzle. The isosurface water VOF does not change much with values between 0.05 and 0.1.

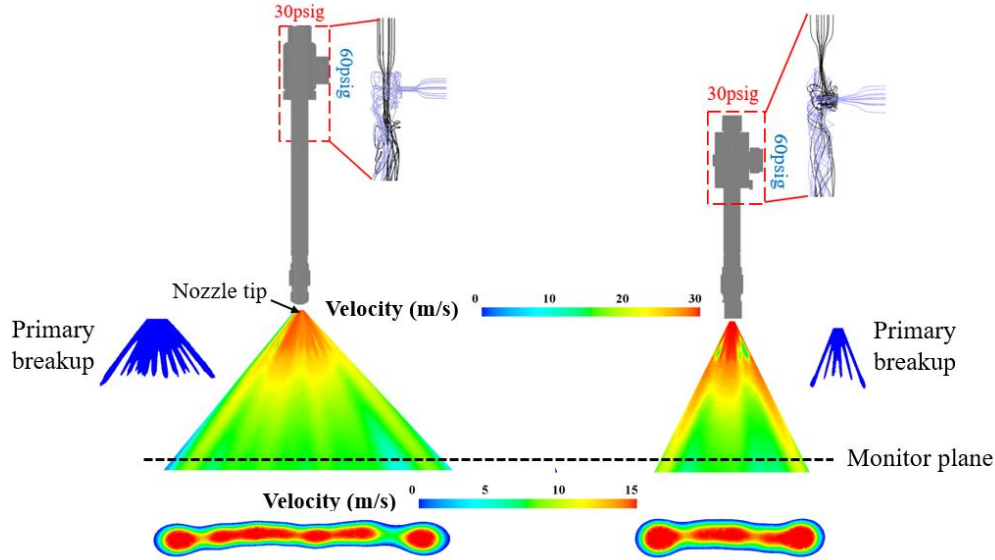


Figure 43. Air-mist nozzles spray characterization.

Spraying System air-mist nozzle shows a smaller water ligament concentrations in the primary breakup. It can result in an improved droplets breakup. Figure 44 plots the sprays coverage showing similar velocities at the monitor plane, yet different effective spray coverage. Simulations were run up to 0.678 seconds. Simulated results for Spraying System air-mist nozzle have not been validated yet. However, results show realistic magnitude values close as reported in [9]. A new simulation using the droplets generation methods covered before can be now added.

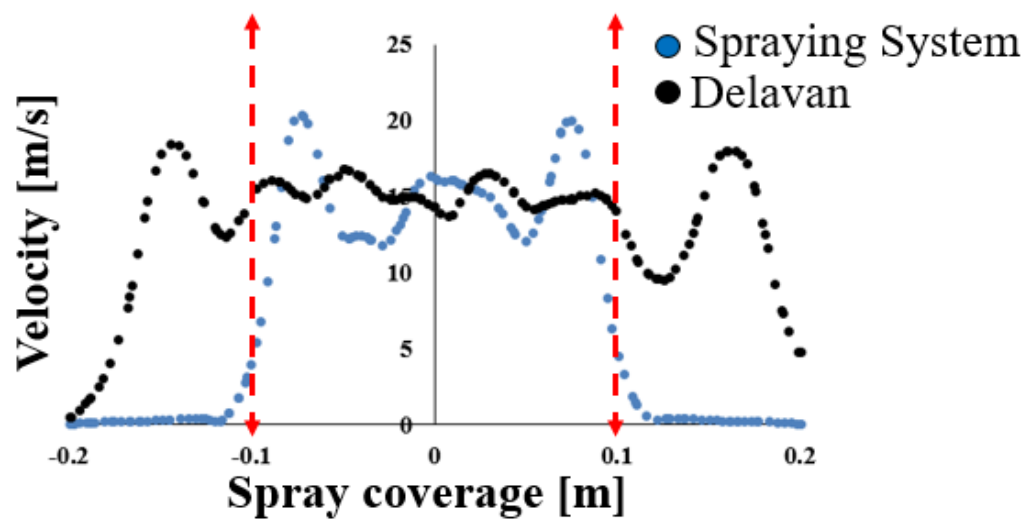


Figure 44. Spray coverage at 190mm standoff distance.

CHAPTER 6. CONCLUSIONS

6.1 Cross-flow simulation

Computational time changes depending on the turbulence model, mesh adaptation method, and mesh resolution being used, which is related to the level of accuracy in droplet size needed. A combination of PUMA and WMLES S-Omega showed good results for validation. PUMA consumed less memory while running simulations and WMLES S-Omega was more suitable to better predict the transition from VOF-to-DPM capturing larger and smaller eddies during the transient gas-liquid interaction.

6.2 Air-mist nozzle simulation

This research focused on the validation of droplets size and droplets velocity magnitude in air-mist nozzles. Understanding water droplets behavior is very important because they will eventually impinge the hot steel slab with a certain mass and momentum, the same ones that are critical for heat removal. A methodology to simulate a complete air-mist spray has been proposed using Computational Fluid Dynamics (CFD) simulations. The whole atomization process study can be broken into three independent but linked sections by considering the computational time. A dispersed VOF interface scheme was chosen to simplify the process as if there is no sharp separation of phases inside the nozzle. Air-mist nozzle spray characterization can be simulated using an Implicit VOF-Compressive interface scheme. Where it was found that if air pressure increases, then the droplet velocity will increase. If water pressure increases, then the droplet velocity will decrease. Energy consumption should be balanced in practice. Two methods to generate liquid droplets were analyzed. First, consideration of mesh density is important if the VOF-to-DPM transition model is planned to be used. The spraying domain could be simulated by using either a grid adaptive method or by having a constant cell size close to the droplet size of interest. Second, the Nukiyama-Tanasawa distribution equation model showed less percentage difference compared to the VOF-to-DPM transition model when validating models to the test data.

REFERENCES

- [1] Morelli, U. (2019, September 4). Continuous casting - Modern techniques to solve an old industrial problem. ROMSOC. Retrieved from <https://www.romsoc.eu/continuous-casting-modern-techniques-to-solve-an-old-industrial-problem/>
- [2] Spraying Systems Co. Drop Size Comparison Between Hydraulic and Air Mist Nozzles. Spray technology for steel mills, B-6. Retrieved from https://www.spray.com/-/media/DAM/Sales-Materials/c/C44B_Spray-Technology-for-Steel-Mills.pdf
- [3] Horsky, J., Raudensky, M., & Tseng, A. A. (2005). Heat Transfer Study of Secondary Cooling in Continuous Casting. AISTech.
- [4] TSI. (2019). A sample of phase dropper measurement - Applications providing flexibility and versatility. Retrieved from <https://www.tsi.com/getmedia/3e826f9d-8f05-49e4-9370-3d32b3fe97da/PDPA%20Applications5001236?ext=.pdf>
- [5] Schick, R. J. (2008). Spray technology reference guide: Understanding drop size. Spraying Systems Co., 16.
- [6] Horsky, J., Raudensky, M., Moravec, R., & Blazek, K. (2015). Heat transfer coefficients for the secondary cooling zones in a continuous casting with the effect of steel chemistry. Ocelary Steelcon.
- [7] Frick, J. Important design parameters and user-friendly features of modern air mist nozzles for slab and beam blank casters. Lecher. Retrieved from https://www.lechler.com/fileadmin/media/fachberichte/metallurgy/lechler_fachbericht_sekundaerkuehlung_important-design-parameters-and-user-friendly-features-of-modern-air-mist-nozzles-for-slab-and-beam-blank-casters_jfrick_en.pdf
- [8] Ramstorfer, F., Roland, J., Chimani, C., & Morwald, K. (2009). Modelling of air-mist spray cooling heat transfer for continuous slab casting. International Journal of Cast Metals Research, 22:1-4, 39-42, DOI: 10.1179/136404609X367290.
- [9] Zhang, Y., Wen, Z., Zhao, Z., Huang, J., Wu, W., & Li, B. (2019). Velocity characteristics of air-mist jet during secondary cooling of continuous casting using PIV and LDV. ISIJ International, 59(6), 1072-1080, DOI: <https://doi.org/10.2355/isijinternational.ISIJINT-2018-735>

- [10] Cheng, C., Wei, S., Li, Y., Zhou, Y., Qin, X., & Zhu, C. (2019). Study of water droplet behavior at air-water atomized nozzle with acceleration ring in continuous casting. STEELSIM, DOI 10.33313/503/063.
- [11] Vashahi, F., Dafsari R. A., Rezaei, S., & Lee, J. (2017). CFD simulation of Two-Phase Flow behavior of a Hybrid Pressure Swirl Atomizer. BEXCO Spring Conference.
- [12] Arthur, H., & Vincent G. (2017). Atomization and Sprays. (2nd ed.). Boca Raton, FL: CRC Press.
- [13] Simcenter. (2019). STAR-CCM+ Multiphase Models, 67.
- [14] Mugele, R. A., & Evans, H. D. (1951, June). Droplet size distribution in sprays. Industrial and Engineering Chemistry.
- [15] Xianguo, L., & Richard S. (1987). Droplet size distribution: A derivation of a Nukiyama-Tanasawa type distribution function. Journal of Combust. Sci. and Tech, 56, 65-76, <https://doi.org/10.1080/00102208708947081>
- [16] Gonzales-Tello, P., Camacho F., Vacaria J., & Gonzalez P. (2008, September 10). A modified Nukiyama–Tanasawa distribution function and a Rosin–Rammler model for the particle-size-distribution analysis. Journal of Powder Technology, 186(3), 278-281, <https://doi.org/10.1016/j.powtec.2007.12.011>
- [17] Hebert, D. A., Schmidt, D. P., Knaus, D. A., Phillips, S., & Magari. P. J. (2008). Parallel VOF spray droplet identification in an unstructured grid. ILASS Americas, 21st Annual Conference on Liquid Atomization and Spray Systems.
- [18] Xiaoyi, L., Arienti, M., Marcos S., Soteriou, M. C., & Sussman, M. M. (2010). Towards an efficient, high-fidelity methodology for liquid jet atomization computations. American Institute of Aeronautics and Astronautics.
- [19] Sami, M., Schuetze, J., Hutchinson, P., & Ozarkar, S. (2019). Efficiently modeling primary liquid atomization using an Eulerian-Lagrangian hybrid model in ANSYS Fluent. ANSYS. Retrieved from https://mfix.netl.doe.gov/workshop-files/2019/Presentations/NETL_Aug_7/Session_6/05-Efficiently_Modeling_Primary_Liquid_Atomization_Using_an_E-L_Hybrid/Efficiently_Modeling_Primary_Liquid_Atomization_Using_an_E-L_Hybrid.pdf
- [20] Sami, M. (2018, May 31). VOF-Lagrangian hybrid spray modeling. ANSYS webinar. Retrieved from <http://storage.ansys.com/webinar/180531-c6f9.mp4>

- [21] Fluent Inc. (2001, November 28). Chapter 23. Grid adaptation. Retrieved from <https://www.afs.enea.it/fluent/Public/Fluent-Doc/PDF/chp23.pdf>
- [22] ANSYS FLUENT 19.1 theory guide.
- [23] Symscape. (2013). Polyhedral, Tetrahedral, and Hexahedral mesh comparison. Retrieved from <https://www.symscape.com/polyhedral-tetrahedral-hexahedral-mesh-comparison>
- [24] STAR-CCM+ 13.04.010 theory guide.
- [25] ANSYS. (2010, December). Lecture 6 Turbulence modeling. Release 13.0. Retrieved from https://imechanica.org/files/fluent_13.0_lecture06-turbulence.pdf
- [26] Reitz, R. (1987). Modeling atomization processes in high-pressure vaporizing sprays. *Atomization and Spray Technology*, 3(4), 309-337.
- [27] Liu, A. B., Mather, D., & Reitz, R. D. (1993). Modeling the effects of drop drag and break up on fuel sprays (No. TP-930072). Wisconsin Univ-Madison engine research center.
- [28] Leong, M. Y., & Hautman, D. J. (2002). ILASS Americas, 15th Annual Conference on Liquid Atomization and Spray Systems.
- [29] Engineering ToolBox. (2004). Air - Density at varying pressure and constant temperatures. Retrieved from https://www.engineeringtoolbox.com/air-temperature-pressure-density-d_771.html
- [30] Wikimedia Commons. Air dry dynamics on pressure temperature. Retrieved from https://commons.wikimedia.org/wiki/File:Air_dry_dynamic_viscosity_on_pressure_temperature.svg
- [31] Spivey, R.J. (2011). A biotic cosmos demystified. ResearchGate.
- [32] Water structure and science. Explanation of the physical anomalies of water F1-F9. Retrieved from http://www1.lsbu.ac.uk/php-cgiwrap/water/pfp.php3?page=http://www1.lsbu.ac.uk/water/physical_anomalies.html
- [33] Engineering ToolBox. (2004). Surface tension of water in contact with air. Retrieved from https://www.engineeringtoolbox.com/water-surface-tension-d_597.html

APPENDIX A. MATLAB CODE FOR INTERPOLATION FLUID-GAS PROPERTIES

Fluid-Gas properties

Density and viscosity properties inputs for running CFD simulations are important to generate realistic flow outcomes. Sometimes simulations results will depend on temperature, pressure among other variables, so it is significant to add an accurate user-defined function that can numerically solve right the properties. This section will give an insight into using different interpolation methods and comparing them to see which one gives a lower percentage difference. Because air is compressed during an air-mist spray process, then it is a must to calculate the corresponding gas properties based on operating pressure conditions, refer to Table 5 for operating conditions in psig units. The laboratory tests by Industrial collaborators, which simulations are based on, were conducted at room temperature. The air properties are pressure dependant as seen in Figure A. 1 and Figure A. 2. Both figures data were extracted using WebPlotDigizer from [29] -- [30] .

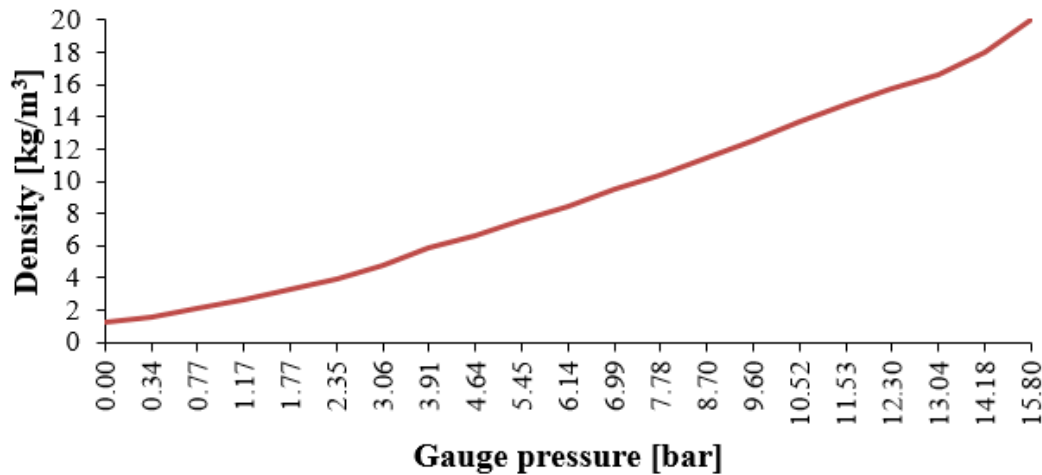


Figure A. 1. Air density vs gauge pressure.

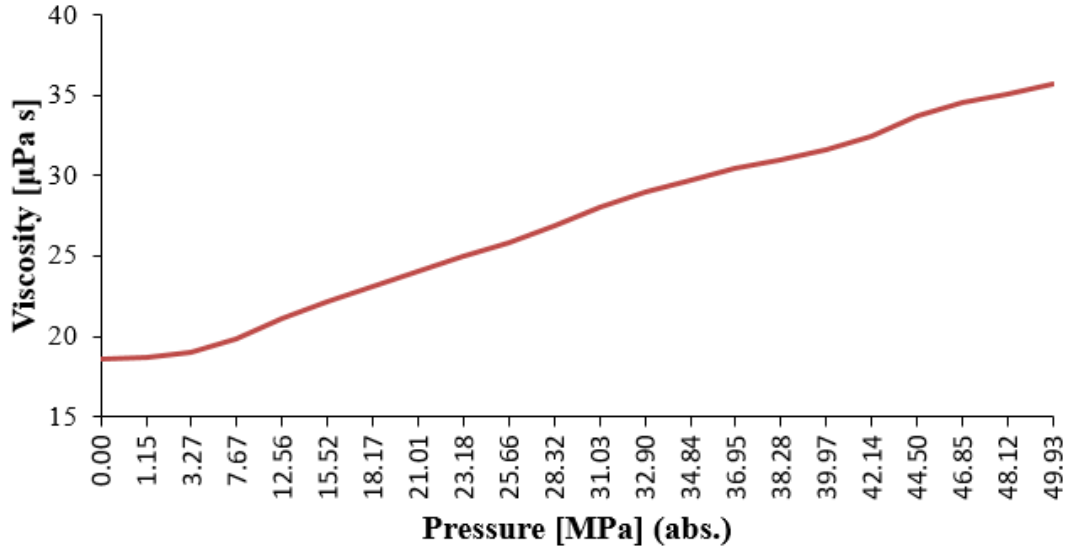


Figure A. 2. Air viscosity vs absolute pressure.

Figure A. 3 shows the comparison of different interpolation methods to calculate air density based on pressure. Excel provides different trendlines and the polynomial 2nd and 6th orders were compared. The percentages different are relatively large. Therefore, MATLAB code was used and exponential least squares and linear least squares methods show lower percentages. The same comparison can be done with other properties and choosing the simpler but the most accurate expression can be accomplished. This analysis is important if a user-defined function is needed to be implemented during the simulation or as in this research to interpolate a constant but accurate value based on pressure operating conditions.

Interpolation Methods									
		2nd polynomial			6th polynomial			Exponential least squares	
		$y=ax^2+bx+c$			$y=ax^6+bx^5+cx^4+dx^3+ex^2+fx+g$			$y=a*\exp(b*x)$	
Pressure abs. (Pa)	Nominal Density (kg/m ³)	Density Approx.	%diff.		Density Approx.	%diff.		Density Approx.	%diff.
101325	1.26	2.25	79.00		2.26	79.64		2.39	90.11
135412	1.60	2.59	62.32		2.60	63.00		2.52	58.05
178180	2.14	3.02	41.15		3.03	41.86		2.70	26.27
218814	2.61	3.43	31.09		3.45	31.87		2.88	10.25
278699	3.29	4.03	22.33		4.06	23.24		3.17	3.68
336442	3.97	4.61	16.05		4.65	17.07		3.48	12.41
407019	4.79	5.32	11.14		5.38	12.30		3.90	18.63
492559	5.84	6.18	5.89		6.26	7.17		4.47	23.51
565281	6.62	6.92	4.50		7.01	5.90		5.02	24.20
646546	7.61	7.74	1.78		7.85	3.26		5.72	24.85
714974	8.49	8.44	0.63		8.56	0.89		6.38	24.87
800521	9.47	9.30	1.79		9.45	0.20		7.31	22.80
879656	10.36	10.11	2.39		10.28	0.74		8.30	19.85
971617	11.44	11.05	3.48		11.24	1.76		9.62	15.95
1061436	12.53	11.96	4.53		12.19	2.75		11.10	11.38
1153389	13.68	12.90	5.72		13.16	3.84		12.87	5.99
1253912	14.80	13.93	5.90		14.23	3.89		15.11	2.07
1330898	15.76	14.72	6.57		15.06	4.44		17.09	8.48
1405750	16.64	15.49	6.90		15.86	4.65		19.27	15.80
1519091	18.03	16.66	7.62		17.09	5.20		23.10	28.12
1681625	20.00	18.33	8.33		18.85	5.74		29.96	49.82
								Linear least squares	
								$y=ax+b$	%diff.
								Density Approx.	%diff.
								1.19	5.29
								1.59	0.13
								2.10	1.81
								2.58	1.25
								3.29	0.07
								3.98	0.07
								4.81	0.50
								5.83	0.26
								6.69	0.99
								7.65	0.58
								8.46	0.33
								9.47	0.01
								10.41	0.54
								11.50	0.51
								12.57	0.29
								13.66	0.21
								14.85	0.28
								15.76	0.02
								16.65	0.04
								17.99	0.23
								19.91	0.43

Figure A. 3. Interpolations methods for air density based on pressure.

```
%%MATLAB CODE
```

```
%% air density
```

```
clear all
```

```
clc
```

```
x=[101325.00
```

```
135411.74
```

```
178180.12
```

```
218814.45
```

```
278698.91
```

```
336442.05
```

```
407018.60
```

```
492559.01
```

```
565280.53
```

```
646545.55
```

```
714973.51
```

```
800521.18
```

```
879655.78
```

```
971616.53
```

```
1061435.96
```

```
1153389.44
```

```
1253911.86
```

```
1330897.86
```

```
1405749.80
```

```
1519091.11
```

```
1681624.79
```

```
];
```

```
y=[1.26
```

```
1.60
```

```
2.14
```

```
2.61
```

```
3.29
```

```
3.97
```

```
4.79
```

```
5.84
```

```
6.62
```

```
7.61
```

```
8.49
```

```
9.47
```

```
10.36
```

```
11.44
```

```
12.53
```

```
13.68
```

```
14.80
```

```

15.76
16.64
18.03
20.00
];
%%explsqr y=a*exp(b*x) air density
explsqr(x,y)
%%linlsqr y=ax+b air density
linlsqr(x,y)

```

```

function explsqr(x,y)
% Construct the least square exponential y=a*exp(b*x)
% that fits x and y row or column vectors.
n=length(x);
n=length(y);
z=log(y);
sumx=sum(x);
sumz=sum(z);
sumx2=sum(x.*x);
sumxz=sum(x.*z);
beta=(n*sumxz-sumx*sumz)/(n*sumx2-sumx^2);
b=beta;
alfa=(sumx2*sumz-sumxz*sumx)/(n*sumx2-sumx^2);
a=exp(alfa);
disp('          Exponential least squares')
fprintf('\n a =%12.16f\n',a)
fprintf(' b =%12.16f\n',b)
disp('_____')
disp(' xi   yi   ln(yi)  a*exp(b*xi)  |yi-[a*exp(b*xi)]|  ')
disp('_____')
for i=1:n
    ye=a*exp(b*x(i));
    err(i)=abs(ye-y(i));
    fprintf('%6.2f %6.2f %6.2f %12.6f %12.6f\n',x(i),y(i),z(i),ye,err(i))
end

```

```

function linlsqr(x,y)
% Construct a least square line y=ax+b
% that fits x and y row or column vectors.
n=length(x);
n=length(y);
sumx=sum(x);

```



```

sumy=sum(y);
sumx2=sum(x.*x);
sumxy=sum(x.*y);
a=(n*sumxy-sumx*sumy)/(n*sumx2-sumx^2);
b=(sumx2*sumy-sumxy*sumx)/(n*sumx2-sumx^2);
disp('          linear least squares')
fprintf('\n a =% 12.16f\n',a)
fprintf(' b =% 12.16f\n',b)
disp('_____')
disp('  x    y    a*x+b    |y-(ax+b)|    ')
disp('_____')
for i=1:n
    yl=a*x(i)+b;
    err(i)=abs(yl-y(i));
    fprintf('%6.2f %6.2f %12.6f %12.6f\n',x(i),y(i),yl,err(i))
end
err=sum(err.*err);
fprintf('\n E(a,b) =%12.6f\n',sum(err))

```

The water properties show less pressure dependant as seen in Figure A. 4 and Figure A. 5. Both figures data were extracted using WebPlotDigizer from [31] -- [32] .

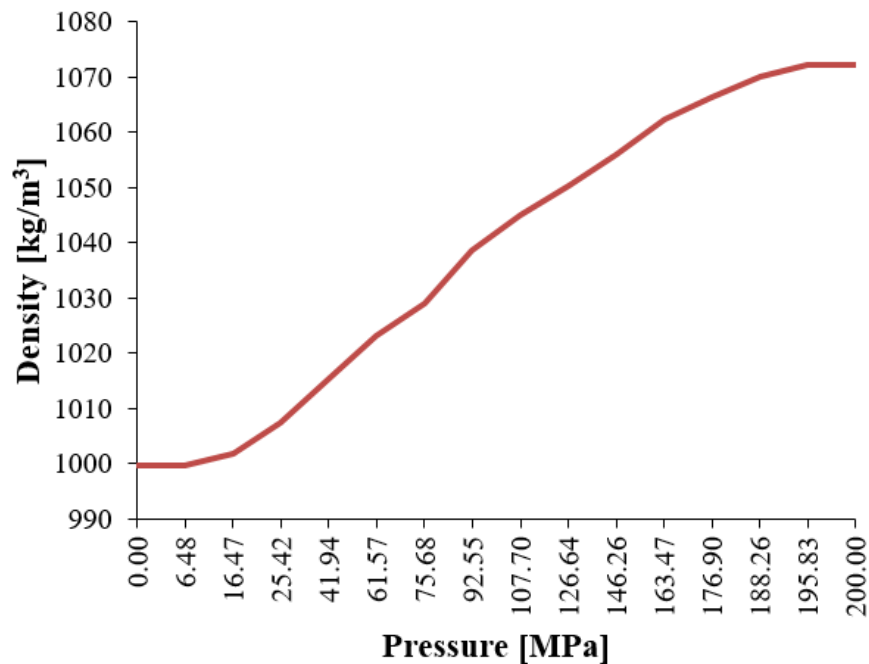


Figure A. 4. Water density vs pressure.

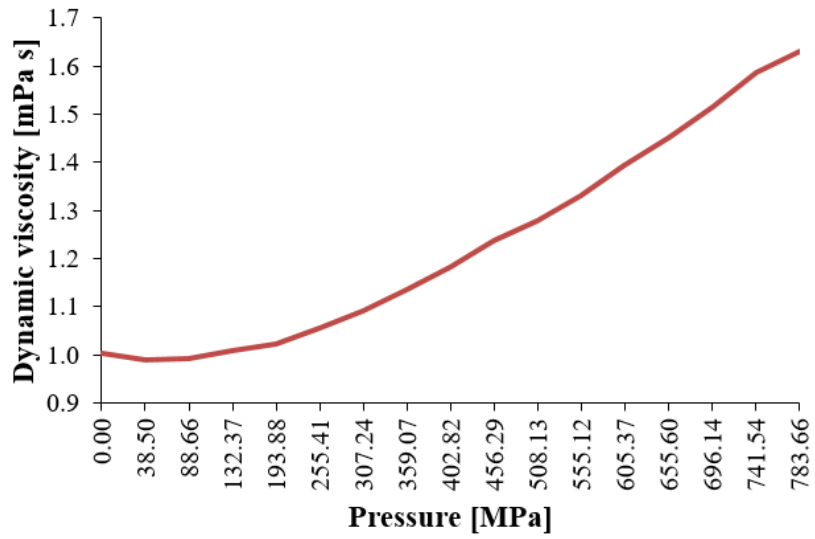


Figure A. 5. Water dynamic viscosity vs pressure.

Because air-mist nozzle has the presence of air and water phases, the surface tension of 0.0724N/m was used as [33] to have a realistic simulation.

APPENDIX B. RATIO APPROXIMATION TO FIND LIMITS IN CUMULATIVE VOLUME SIZE DISTRIBUTION

Based on operating conditions

Typical distribution		Condition 30psig - 4.5GPM				
Typ. size (μm)	Typ. cumulative %	Exp. size (μm)	Ratio (Typ. size/Exp.size)	Avr.ratio	Approx. (Typ. size/Avr. ratio)	% diff. Exp & Appro.
1.71	0			0.21	8	
12.52	3				59	
16.70	10	75	0.22		79	4.87
25.69	29				121	
34.60	50	170	0.20		163	4.15
42.43	65				200	
49.94	76				235	
62.19	87				293	
68.30	90	324	0.21		322	0.72
85.38	95				402	
104.09	99				490	
119.77	99				564	
124.60	100				587	

Figure B. 1. Size distribution for 30psig – 4.5GPM.

Typical distribution		Condition 40psig - 4.5GPM				
Typ. size (μm)	Typ. cumulative %	Exp. size (μm)	Ratio (Typ. size/Exp.size)	Avr.ratio	Approx. (Typ. size/Avr. ratio)	% diff. Exp & Appro.
1.71	0			0.28	6	
12.52	3				44	
16.70	10	56	0.30		59	5.82
25.69	29				91	
34.60	50	130	0.27		123	5.56
42.43	65				151	
49.94	76				177	
62.19	87				221	
68.30	90	243	0.28		242	0.26
85.38	95				303	
104.09	99				369	
119.77	99				425	
124.60	100				442	

Figure B. 2. Size distribution for 40psig – 4.5GPM.

Typical distribution		Condition 30psig - 6.5GPM				
Typ. size (μm)	Typ. cumulative %	Exp. size (μm)	Ratio (Typ. size/Exp.size)	Avr.ratio	Approx. (Typ. size/Avr. ratio)	% diff. Exp & Appro.
1.71	0			0.12	14	
12.52	3				104	
16.70	10	132	0.13		139	5.57
25.69	29				214	
34.60	50	308	0.11		289	6.26
42.43	65				354	
49.94	76				417	
62.19	87				519	
68.30	90	566	0.12		570	0.69
85.38	95				712	
104.09	99				869	
119.77	99				999	
124.60	100				1040	

Figure B. 3. Size distribution for 30psig – 6.5GPM.

Typical distribution		Condition 40psig - 6.5GPM				
Typ. size (μm)	Typ. cumulative %	Exp. size (μm)	Ratio (Typ. size/Exp.size)	Avr.ratio	Approx. (Typ. size/Avr. ratio)	% diff. Exp & Appro.
1.71	0			0.17	10	
12.52	3				75	
16.70	10	94	0.18		100	6.91
25.69	29				155	
34.60	50	215	0.16		208	3.16
42.43	65				255	
49.94	76				301	
62.19	87				374	
68.30	90	427	0.16		411	3.75
85.38	95				514	
104.09	99				626	
119.77	99				721	
124.60	100				750	

Figure B. 4. Size distribution for 40psig – 6.5GPM.

PUBLICATIONS

Mosquera E, et al. Numerical Model Development for Air-mist Spray in Steel Secondary Cooling Process Using the VOF-to-DPM Multiphase Transition Model [C] AIST 2020 (published)

Moreland J, Estrada J, Mosquera E, et al. Integrating Fluid Simulation with Virtual Die Casting Machine for Industry 4.0 and Operator Training [C] TMS 2020 (published)